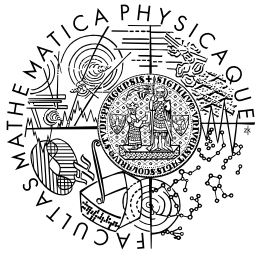

FACULTY
OF MATHEMATICS
AND PHYSICS
Charles University

MASTER THESIS

Adam Strnad

Investigation of phase transformations in ternary zirconium alloys

Department of Physics of Materials

Supervisor of the master thesis: RNDr. Jana Šmilauerová, Ph.D.

Study programme: Physics of Condensed Matter and Materials

Prague 2024

I declare that I carried out this master thesis on my own, and only with the cited sources, literature and other professional sources. I understand that my work relates to the rights and obligations under the Act No. 121/2000 Sb., the Copyright Act, as amended, in particular the fact that the Charles University has the right to conclude a license agreement on the use of this work as a school work pursuant to Section 60 subsection 1 of the Copyright Act.

In ..... date ....

Author's signature

I would like to thank my supervisor, RN Dr. Jana Šmilauerová, Ph.D., for her guidance and support during my master studies. I would also like to thank her for the assistance and encouragement she provided while I wrote this thesis. I would like to thank my colleagues from the Department of Physics of Materials, namely RNDr. Dalibor Preisler, Ph.D., for introducing me to X-ray diffraction and RNDr. Petr Harcuba, Ph.D., for the guidance and expertise he provided while I was working with a scanning electron microscope.

Title: Investigation of phase transformations in ternary zirconium alloys
Author: Adam Strnad
Department: Department of Physics of Materials
Supervisor: RNDr. Jana Šmilauerová, Ph.D., Department of Physics of Materials

Abstract: In this thesis, we studied phase transformations, microstructure, and mechanical properties of two newly designed alloys, Zr-4Sn-1Cr and Zr-4Nb-2Al (in wt%). Phase transformations were investigated, employing differential scanning calorimetry (DSC) and electric resistance measurements. The microstructure and phase composition were investigated using scanning electron microscopy (SEM) and X-ray diffraction analysis (XRD) in the cast+homogenized state and after various heat treatments. We studied the evolution of Zr_2Cr particles in the alloy Zr-4Sn-1Cr and observed the precipitation of intermetallic Zr_2Al and Zr_3Al phases in the alloy Zr-4Nb-2Al. We performed hot swaging of the studied alloys and investigated their mechanical properties using microhardness and tensile measurements. Both swaged alloys achieved higher ultimate tensile strength than commercially used Zircaloy-2 and Zircaloy-4.

Keywords: zirconium alloys, phase transformations, mechanical properties, thermomechanical processing

Název práce: Studium fázových transformací v ternárních slitinách zirkonia
Autor: Adam Strnad
Katedra: Katedra fyziky materiálů
Vedoucí diplomové práce: RNDr. Jana Šmilauerová, Ph.D., Katedra fyziky materiálů

Abstrakt: V předložené práci byly studovány fázové transformace, mikrostruktura a mechanické vlastnosti dvou nově navržených slitin, Zr-4Sn-1Cr a Zr-4Nb-2Al (v hmotnostních %). Fázové transformace byly zkoumány pomocí diferenční skenovací kalorimetrie (DSC) a měřením elektrického odporu. Mikrostruktura a fázové složení byly zkoumány pomocí skenovací elektronové mikroskopie (SEM) a rentgenové difrakční analýzy (XRD) v odlitém + homogenizovaném stavu a po různých tepelných zpracováních. Studovali jsme vývoj Zr_2Cr částic ve slitině Zr-4Sn-1Cr a pozorovali výskyt precipitátů intermetalických fází Z_2Al a Zr_3Al ve slitině Zr-4Nb-2Al. Provedli jsme horké rotační kování studovaných slitin a zkoumali jejich mechanické vlastnosti pomocí mikrotvrdostních a tahových zkoušek. Obě vykované slitiny dosáhly při tahových zkouškách vyšší meze pevnosti než komerčně používané zirkoniové slitiny Zircaloy-2 a Zircaloy-4.

Klíčová slova: zirkoniové slitiny, fázové transformace, mechanické vlastnosti, termomechanické zpracování

Contents

Introduction

Zirconium, a lustrous, grayish-white transition metal, has attracted significant attention in materials science and engineering due to its remarkable properties and versatile applications. With their excellent corrosion resistance, low neutron absorption cross-section, and outstanding mechanical properties, zirconium and its alloys have become indispensable in various industrial sectors, ranging from nuclear reactors to biomedical implants [1].

One of the most notable features of zirconium is its exceptional corrosion resistance, attributed to the formation of a stable oxide layer on its surface. This inherent property makes zirconium alloys highly desirable for applications where exposure to aggressive environments, such as high temperatures and corrosive chemicals, is commonplace [2]. Moreover, the mechanical properties of zirconium, including high strength, ductility, and thermal stability, make it indispensable in the aerospace and automotive industries [3].

Additionally, the low neutron absorption cross-section of zirconium makes it an ideal material for nuclear reactor components, facilitating efficient energy production while ensuring safety and reliability [4].

Currently, there is a tendency for the development of zirconium alloys with enhanced mechanical properties. Structural components made from mechanically stronger alloys decrease the cost and increase the safety of nuclear reactors. Using such a material would make nuclear reactors more stable during regular operation, as well as during accidents in which the stress on individual components is increased. Therefore, the development of zirconium alloys with better mechanical properties is a way to improve the efficiency and safety of nuclear reactors [5].

The zirconium alloys in modern reactors contain a relatively low amount of alloying elements. Commonly used Zircaloy-2 and Zircaloy-4 contain less than 1.5 wt% tin and less 0.2 wt% chromium and iron. The advantage of low alloyed zirconium is that the low cross section for neutrons is maintained. On the other hand, strengthening mechanisms such as solid solution and precipitation hardening are not fully utilized.

It was shown that a microstructure containing both α and β phases produces excellent mechanical properties [6]. An example of this microstructure is the widely used titanium alloy Ti-6Al-4V with excellent mechanical properties, which is utilized in a variety of fields from aerospace to biomedicine [7].

With all these factors in mind, new zirconium alloys were developed at the Department of Physics of Materials at Charles University: Zr-4Sn-1Cr and Zr-4Nb-2Al (in wt%). These ternary alloys contain both α (Sn, Al) and β stabilizers (Nb, Cr) in higher amounts than commercial alloys. The main objective was to design a composition that would lead to high material strengthening and favorable microstructure.

1 Literature review

1.1 Phase composition of Zirconium and its alloys

A variety of different phases exist in zirconium and its alloys. They are divided based on thermodynamic stability into equilibrium phases, which exist in thermodynamic equilibrium, and non-equilibrium phases. The existence of equilibrium phases depends on composition, temperature, and pressure and can be described by an equilibrium phase diagram. Non-equilibrium phases exist in the material when a rapid change, for example quenching, prevents the establishment of an equilibrium state.

1.1.1 Equilibrium phases

At room temperature and normal pressure, zirconium crystalizes in the hexagonal close-packed (hcp) α phase. It is a crystal structure of the $P6_3/mmc$ space group with lattice parameters $a = 3.2316$ Å and $c = 5.1475$ Å (figure 1.1). When the temperature is raised above 865 °C, the α transforms to the body-centered cubic (bcc) β phase, which is of the $Im\bar{3}m$ space group with the lattice parameter $a = 3.61$ Å (figure 1.2). The addition of alloying elements to zirconium usually changes the temperature of this transformation. Some elements raise the temperature of $\alpha \rightarrow \beta$ transformation and stabilize the α phase. Other elements allow the β phase to exist in equilibrium at lower temperatures by lowering the temperature of the transformation. This property is the main criterion by which we divide the alloying elements in zirconium alloys. Elements that increase the temperature of this transformation are called α stabilizers. Elements with this property are usually non-transition metals such as Al, Sn, and interstitial elements like O, C, and N. On the other hand, elements decreasing the temperature are called β stabilizers. These are usually transition metals like Cr, Nb, and noble metals with unfilled or just-filled d-electron bands. Another notable β stabilizer is hydrogen, which usually occupies interstitial positions in the α or β crystal lattice [8].

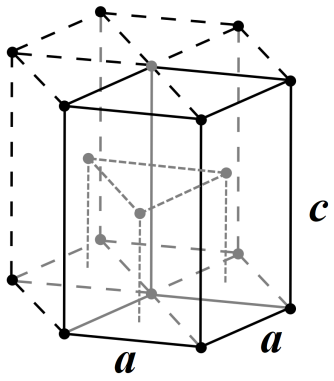

Figure 1.1 Hexagonal close-packed crystal structure [9].

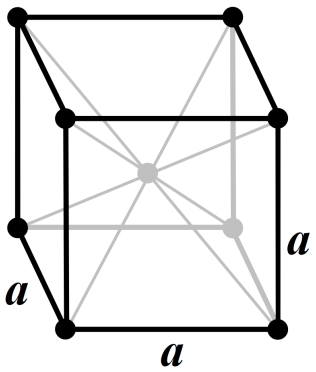

Figure 1.2 Body centred cubic crystal structure [10].

In zirconium alloys, in which the number of chemical components is at least two, α and β can coexist in an equilibrium. Regions in the phase diagram where only α or β exist are separated by an α+β coexistence region. The range of temperatures in which these phases exist in equilibrium generally increases with the addition of solute atoms. There are two important equilibrium temperatures: the α transus temperature, below which only α exists, and the β transus temperature, above which only β exists [8].

Apart from α and β, other equilibrium phases are found in Zr alloys. At high pressures and low temperatures, the equilibrium ω phase exists (see figure 1.3). It has a hexagonal crystal lattice with P6/mmm symmetry group and lattice parameters $a = 5.036\,\text{Å}$ and $c = 3.109\,\text{Å}$. Another group of equilibrium phases that form in zirconium alloys are called intermetallic phases. In a phase diagram, they appear in between the phases of the pure elements and form a variety of orderer and disordered crystal structures. The types of intermetallic phases and the causes of their formation will be further discussed in chapter 1.2, and examples of intermetallics from relevant Zr-X systems will be presented in chapter 1.3.

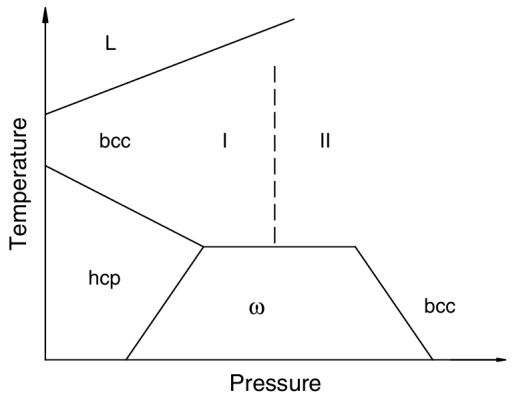

Figure 1.3 Phase diagram of elemental zirconium [8].

1.1.2 Non-equilibrium phases

Non-equilibrium phases form when a rapid change, such as rapid cooling, prevents the establishment of equilibrium. Important non-equilibrium phases in zirconium and its alloys are the martensitic phases and the athermal ω. There is an important distinction between athermal ω and equilibrium ω mentioned in the previous section. The equilibrium ω exists only at high pressures, while athermal omega forms during quenching of the β phase in highly β stabilized alloys and can exist in a metastable state in ambient conditions.

If an alloy contains sufficient amounts of β stabilizing elements, a transformation from β to martensitic phase may occur during rapid quenching. The martensite phase forms during a martensitic transformation, a diffusionless transformation involving a cooperative movement of atoms throughout the material. Depending on the composition of the alloy, this martensite may either be hcp α' or orthorhombic α''. If only moderate amounts of β stabilizing elements are present in the parent β, the α' martensite is formed. When a higher content of β stabilizing elements is present, the α'' martensite forms [8].

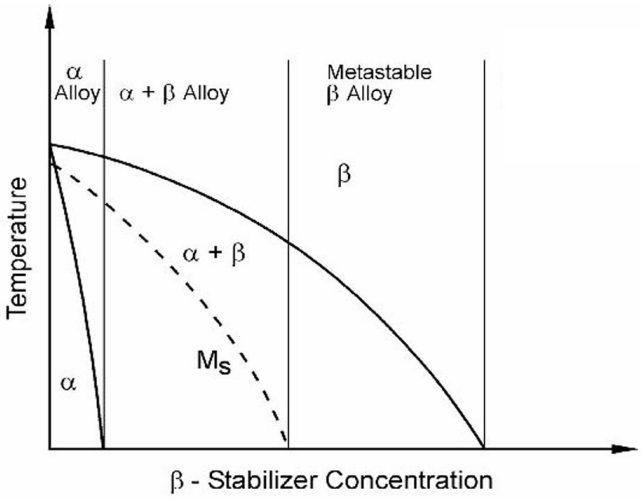

Figure 1.4 Classification of zirconium alloys [12].

During martensitic transformation, the crystal lattice must undergo high deformations. For this reason, the start of martensitic transformation is not exactly at temperature T_0 in which the Gibbs energy of the martensite and the β phase are equal. Sufficient undercooling must be present in order for the driving force of the transformation to overcome the energy barrier. The temperature where this condition is satisfied and martensitic transformation starts is called martensite start temperature M_s and is usually 50 °C below the T_0 [11].

The presence of martensite in quenched zirconium alloys plays an important role in the classification of Zr alloys. Alloys which contain only α phase in equilibrium at temperatures around 600 °C are called α zirconium alloys. Alloys that contain α' or α'' martensite after quenching from the β phase, are called $\alpha + \beta$ alloys. Finally, alloys that retain a fraction of the β phase after quenching are called metastable β alloys (see figure 1.4) [8].

1.2 Intermetallic phases

An intermediate phase, or in the case of metallic elements, an intermetallic phase, is a phase of a crystal structure different from the primary phases, which lies between them in the phase diagram. In some cases, the intermetallic phases exist over a large range of compositions; in other cases, they are bound by strict structural constraints and exhibit an exact stoichiometry [13].

Generally speaking, intermetallic phases are hard and brittle, but due to their partial metallic bonding, they are less brittle than ceramics. The brittleness of an intermetallic phase tends to decrease with increasing crystal symmetry and decreasing unit cell size. This allowed some intermetallic phases to be considered as potential structural materials, as in the case of Zr_3Al and Ti_3Al [8].

The structure of intermediate phases is governed by relative electronegativity, valence, and atomic size. We can then distinguish three distinct types of intermediate compounds based on the main reason for their formation: Electrochemical compounds are created due to the attractive bond between highly electropositive and electronegative components. The formation of electron phases is governed

by the electron concentration expressed as the ratio e/a of valence electrons per atom [14]. When the atomic diameters of two elements differ by a large margin, size-factor compounds may be formed. We can distinguish between interstitial and substitutional size-factor compounds. Typical examples of interstitial compounds are borides, hydrides, carbides, and nitrides of the transitional metals. Suppose the ratio between interstitial and metal atom radii exceeds 0.59. In that case, the distortion caused by the interstitial atom becomes significant, and more complex crystal structures may be formed, leading to the formation of substitutional size-factor compounds [13].

1.2.1 Laves phases

In a binary compound in which the two elements have atomic size differences around 20-30%, the Laves phase structure achieves the most efficient packing of atoms. These phases have the formula AB_2, where A atoms are arranged in a hexagonal manner, and B atoms are arranged on a space lattice of tetrahedra (see figure 1.5). In Zr-X systems, these phases crystallize in one of three structures: $ZrCu_2$ with cubic lattice (space group $Fd\bar{3}m$), $ZrZn_2$, and $ZrNi_2$ with hexagonal lattice (space group $P6_3/mmc$) [13]. Phases with structures of these prototypes are generally called C15, C14, and C36 Laves phases, respectively [15].

The smaller atoms are arranged on a space lattice of tetrahedra in all of the Laves phases. The different ways of joining these tetrahedra produce the three different Laves structures. In the C15 structure, the smaller atoms are positioned at the corners of the tetrahedra. The tetrahedra are then connected in space in a way that can be seen in figure 1.5. This arrangement leads to large holes (figure 1.5), which, in the ideal case, are filled with atoms with a size ratio of 1.225 with respect to the smaller atoms. The resulting cubic C15 structure is displayed in figure 1.5b. Another way to describe the Laves structures is as a stacking pattern of two layers $\triangle$ and $\triangledown$, where the second layer is created by a 180° rotation of the first layer. The C14, C15, and C36 structures can then be described by repeating $\triangle$ or $\triangledown$ layers, as can be seen in figure 1.6 [15].

Due to the strict geometrical conditions placed on their structure, the range of composition of the Laves phases is very narrow around the 1:2 stoichiometric ratio [15].

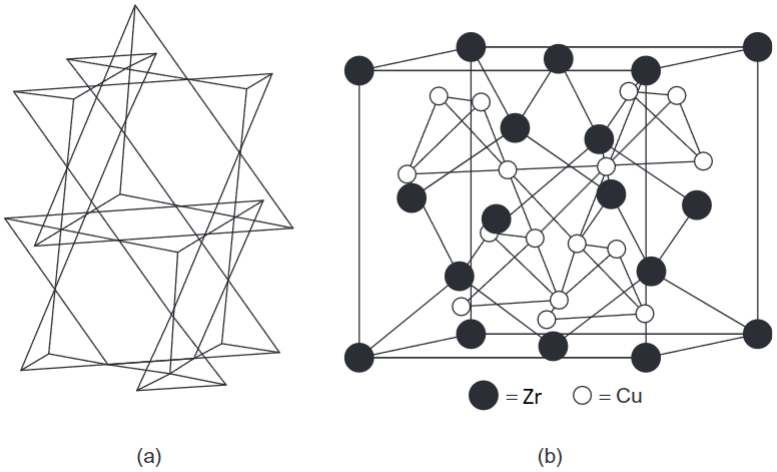

Figure 1.5 Laves $ZrCu_2$ (C15) structure. a) Framework of the $ZrCu_2$ structure. b) Complete $ZrCu_2$ structure [13].

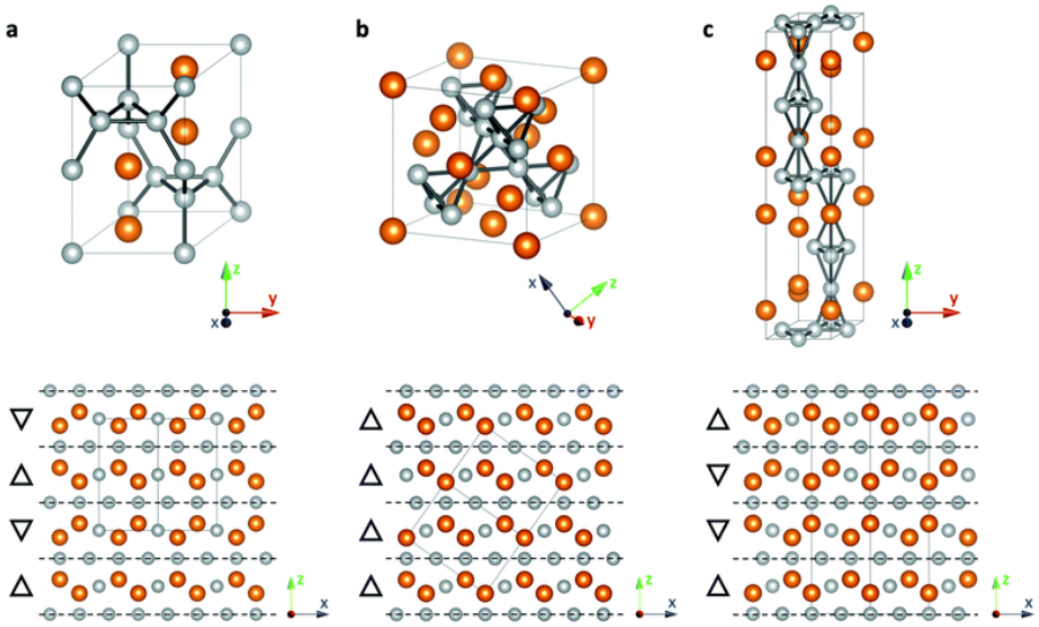

Figure 1.6 Stacking of Laves structures. a) $ZrZn_2$ (C14). b) $ZrCu_2$ (C15). c) $ZrNi_2$ (C36) [15].

1.3 Binary systems Zr-X

1.3.1 Zr-Cr

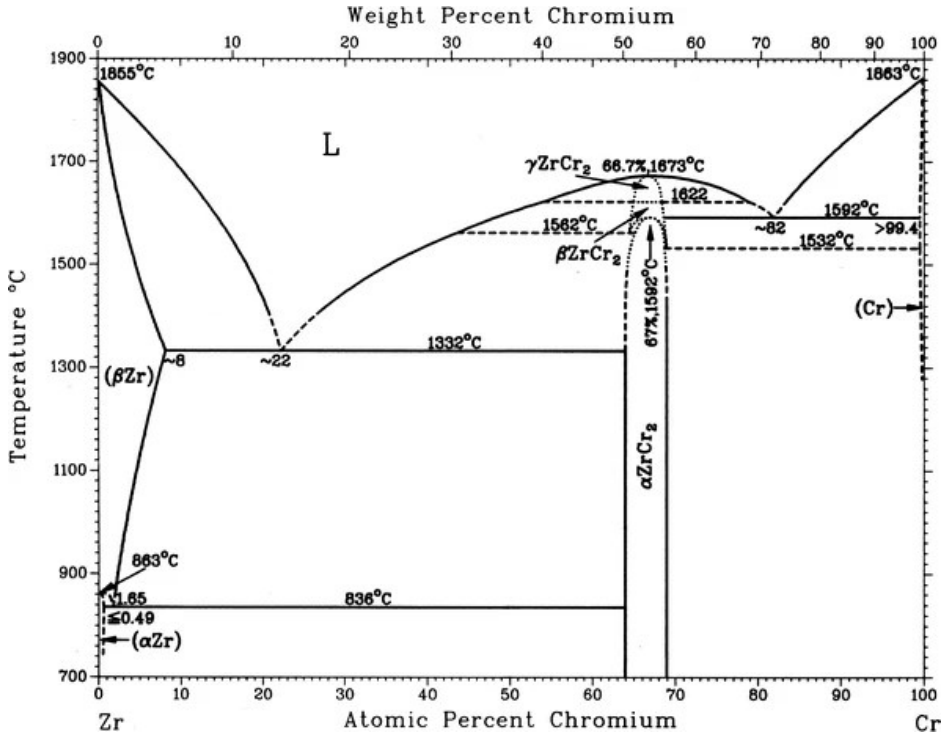

Figure 1.7 Equilibrium diagram of the Zr-Cr system [16].

In the context of zirconium alloys, chromium is a β stabilizing element. When chromium is added to Zr alloy, it will lower the temperature of β transus and increase the retention of the β phase. The phase diagram of the zirconium-chromium system shown in figure 1.7. At low chromium content, the zirconium-chromium system forms solid solutions of hcp α and bcc β phases. The maximum content of chromium soluble in the α phase is relatively low: 0.49 at.% Cr at 863 °C. On the other hand, the β phase might contain up to 8 at.% of chromium [17].

When the terminal solubility of chromium in zirconium is exceeded, three intermetallic Laves phases form in zirconium-chromium alloys. The cubic $\alpha ZrCr_2$ (C15) and two hexagonal phases $\beta ZrCr_2$ (C36) and $\gamma ZrCr_2$ (C14). All of them exist in a narrow composition range around the Zr:2Cr stoichiometry. The $\alpha ZrCr_2$ is stable at low temperatures up to 1592°C, above which it transforms to $\beta ZrCr_2$ (see figure 1.7). The $\beta ZrCr_2$ exists in a narrow temperature range of only about 30 °C and transforms to the $\gamma ZrCr_2$ at around 1622 °C [17].

An important phase transformation for zirconium alloys, where chromium content is usually a few weight percent at most, is the eutectoid transformation $\beta \rightarrow \alpha Zr + \alpha ZrCr_2$. This transformation occurs at a chromium content of 1.65 at.% and temperature of 836 °C. The hcp α precipitates as thick laths within the β grains, and large crystalline $ZrCr_2$ particles form at grain boundaries of the dissolving β grains [18].

The quenching of alloys with less than 1.8wt.%Cr fully suppresses the precipitation of $ZrCr_2$ at the eutectoid temperature and creates a fully martensitic microstructure.

Alloys with more than 2.5 wt.% Cr retain a fraction of the initial β phase upon quenching. In alloys with less chromium, the quenching of the β phase leads to diffusionless transformation to α' martensite. After reheating and aging, the $ZrCr_2$ precipitates, depending on the concentration of chromium, uniformly through the martensite or heterogeneously at twin and martensitic interfaces [19]. At higher concentrations of chromium (3.4 at.% Cr), the metastable ω phase forms upon quenching. If aged under eutectoid temperature, the martensite and ω phases decompose to equilibrium $\alpha + ZrCr_2$ [19].

Chromium is commonly used in commercial Zr alloys; examples are Zircalloy-2 and Zircalloy-4, which contain 0.1 wt% of Cr. Chromium is used due to its positive effect on corrosion resistance and mechanical properties, such as creep resistance and tensile strength [20]. Due to the low solubility of chromium in zirconium, intermetallic particles of $ZrCr_2$ are generally present [5]. The presence of these particles was reported to promote electronic conduction, which leads to higher hydrogen evolution on the oxide-water interface. This results in a lower hydrogen pickup into the material itself [21].

1.3.2 Zr-Sn

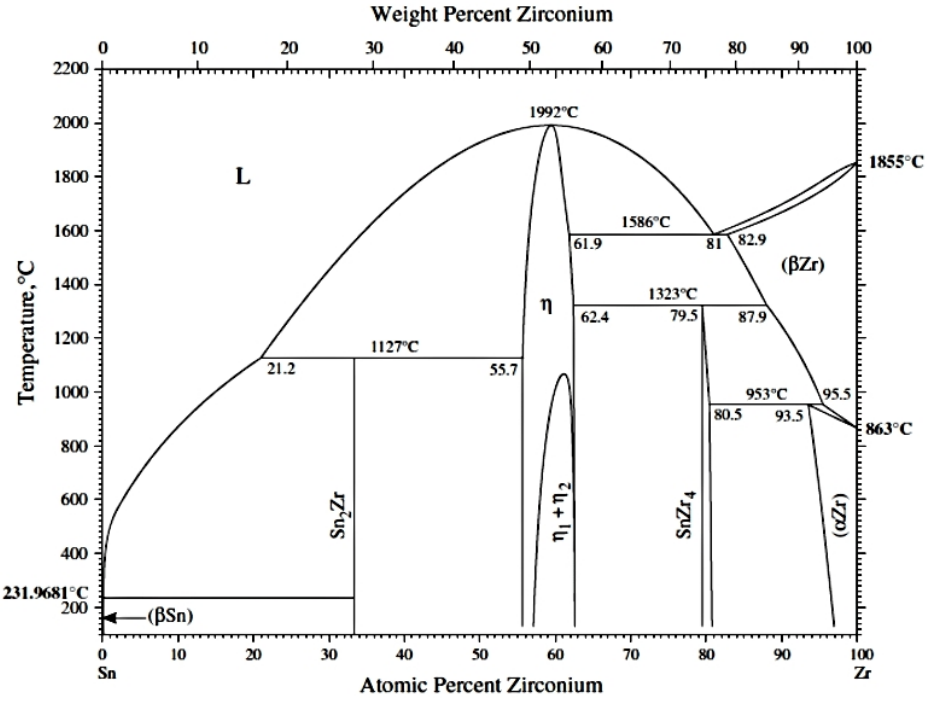

Figure 1.8 Equilibrium diagram of the Zr-Sn system [22].

The zirconium-tin system plays an essential role in commercially used zirconium alloys. In widely used alloys, Zircalloy-2 and Zircalloy-4, tin is the most abundant alloying element, making up to 1.7 wt% of these alloys. It is mainly used to mitigate the adverse effect of N on corrosion resistance and to increase the mechanical properties of the alloys [5]. Furthermore, the addition of Sn leads to an increase in yield strength and creep resistance. The mechanism of increased creep resistance is assumed to be due to the reduction of Zr self-diffusion [23] or by lowering the stacking fault energy [24].

Tin exhibits α stabilizing properties in Zr alloys. In elemental zirconium, tin can increase the stability of α phase from 863 °C up to 953 °C in the Zr-6.5Sn (in wt%) alloy.

If we look at the Zr-Sn phase diagram in figure 1.8, we can see five intermetallic phases: Zr_4Sn, η, η_1, η_2 and $ZrSn_2$. The Zr_4Sn phase has the A15 cubic structure with a typical 3:1 stoichiometry. However, in the case of Zr_4Sn, it exists around the 4Zr:1Sn stoichiometry. The unusual stoichiometry can be explained by the mechanism of how sublattices are occupied. In the A15 structure there are two sublattices, one with three atoms per cell and one with one atom per cell. In most A15 structures, each sublattice is occupied only by one element, leading to a 3:1 composition. In Zr_4Sn, the first sublattice is occupied only by Zr atoms, and the second sublattice is occupied by 20% Zr and 80% Sn atoms, which leads to the 4:1 composition of Zr_4Sn [25].

All of the η phases are strongly related. The η_1 and η_2 have the Zr_5Sn_3 and Zr_5Sn_4 compositions, respectively. Their crystals have the same space symmetry group ($P6_3/mmc$) and, in most cases, the same occupancy of sites in the lattice. Above 1000 °C only one η phase exists with the Zr_5Sn_{3+x} composition, where x is between 0 and 1 [25].

The $ZrSn_2$ phase has the structure of the Si_2Ti prototype, with exact 1:2 stoichiometry.

1.3.3 Zr-Nb

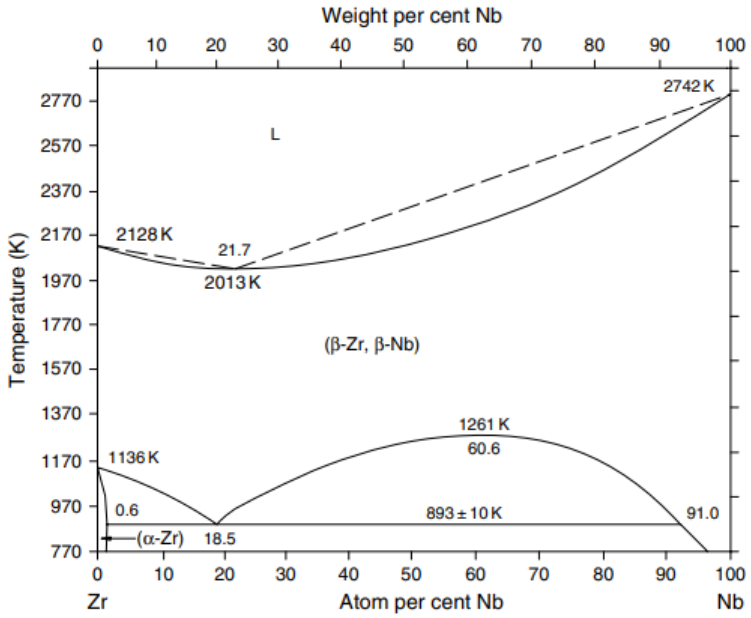

Figure 1.9 Equilibrium diagram of the Zr-Nb system [26].

Niobium is a strongly β stabilizing element, which is evident from the Zr-Nb phase diagram in figure 1.9. The solid solution of bcc β phase exists from 980 °C to 1740 °C at all compositions. The solubility of niobium in α zirconium is very low, with a maximum of around 0.6 wt%. At higher concentrations

and temperatures below 620 °C, the zirconium-rich hcp α and niobium-rich bcc β coexist in an equilibrium [27].

The α' martensite and athermal ω form during quenching from the β phase field. In alloys with less than 7 wt% Nb, all of the β phase transforms to the α' martensite. When the concentration of Nb is increased up to 7.5 wt% Nb, the quenching preserves a portion of the original β, and both the metastable α' martensite a ω phase forms during rapid cooling. In alloys with more than 7.5 wt% Nb, only β and ω phases are present in the alloy after quenching [27].

The martensitic start temperature in pure Zr is at 860 °C. This temperature decreases with an increase in the Nb content. Adding 6 wt% Nb to elemental zirconium can lower the martensitic start temperature below 500 °C [28].

Adding Nb to zirconium alloys for nuclear purposes improves the mechanical properties without a substantial increase in neutron capture cross section. It mainly increases the hardness of the alloy and increases creep resistance. The addition of Nb also decreases the adverse effects of impurities such as N and C [29].

1.3.4 Zr-Al

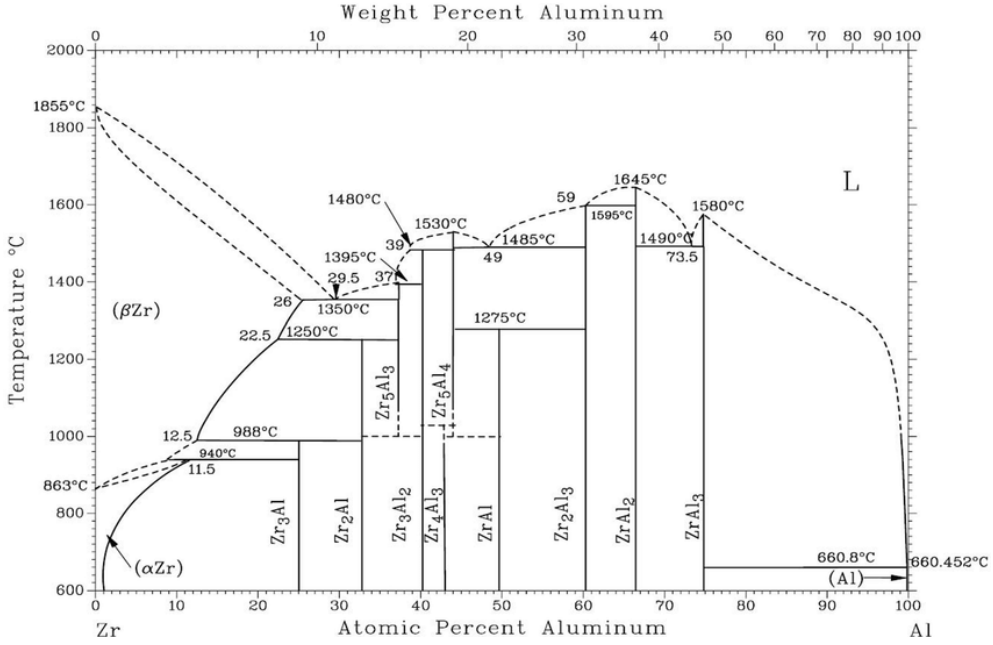

Figure 1.10 Equilibrium diagram of the Zr-Al system [30].

Aluminium is an α stabilizing element. A high number of intermetallic phases is present in the Zr-Al phase diagram (see figure 1.10). We will focus on the zirconium-rich side of the Zr-Al phase diagram, where the Zr_3Al and Zr_2Al are found [30].

The Zr-richest intermetallic phase in the Zr-Al system is the Zr_3Al. It has the cubic structure of the $CuAu_3$ prototype and an exact 3Zr:1Al stoichiometric ratio [31]. At compositions lower than 25 at.% Al, the Zr_3Al coexists with the αZr up to 940 °C; and between 940 °C and 988 °C it coexists with the βZr phase. At the temperature of 988 °C, the Zr_3Al undergoes a peritectoid reaction $Zr_3Al \leftrightarrow \beta Zr + Zr_2Al$, during which the intermetallic Zr_2Al is formed. The Zr_2Al has a hexagonal crystal structure of the $InNi_2$ prototype and an exact 2Zr:1Al stoichiometric ratio [30].

1.3.5 Zr-H

The presence of other elements in zirconium alloys is not always deliberate. Zirconium alloys will always contain elements like oxygen and hydrogen that diffuse to the material during production and operation. One problem related to such contamination is hydrogen-induced embrittlement. The formation of zirconium hydride causes a loss in the ductility of the material, which causes safety issues, mainly in water-cooled nuclear reactors, where zirconium is used as a structural material.

When zirconium alloys are in contact with water, corrosion occurs, and an oxide layer forms on the surface. This leads to the release of hydrogen, which diffuses into the material and forms a solid solution with zirconium. When the maximum hydrogen solubility in zirconium is reached, zirconium hydride starts to precipitate. The precipitation is usually in the form of δ hydride, in which the Zr atoms form a fcc lattice and the H atoms randomly occupy the eight tetrahedral interstitial sites (see figure 1.11). At room temperature, the δ hydride has the stoichiometry $ZrH_{1.59}$ and the lattice parameter $a = 4.778$ Å [32].

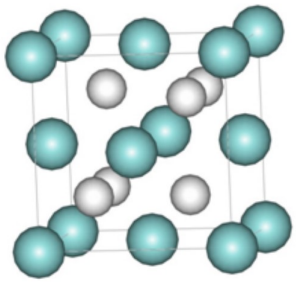

Figure 1.11 Structure of δ zirconium hydride [32].

1.4 Zr alloys in nuclear industry

Zirconium alloys play an indispensable role in the nuclear industry. Its 15 times smaller neutron capture cross-section than steel allows zirconium components in nuclear reactors to be made lighter and smaller. The construction of fuel cladding and other structural components from zirconium alloys decreases the need to enrich uranium fuel, making nuclear energy safer and less expensive. The timeline of zirconium alloys used in nuclear industry is shown in figure 1.12.

Elemental zirconium has low corrosion resistance, which is further lowered by the presence of nitrogen. For this reason, a zirconium alloy named "Zircaloy-2" was developed where Sn, Fe, Cr, and low amounts of O and Ni were used to increase strength and corrosion resistance. Another successful alloy developed was the Zircaloy-4, where no Ni was present, and the amount of Fe was increased to 0.2 wt%. Zircaloy-2 is currently in use in boiling water reactors due to its superior corrosion resistance at elevated temperatures [33]. Zircaloy-4 is used in pressured water reactors due to its lower hydrogen absorption [34].

The addition of Nb instead of Sn also leads to an increase in corrosion resistance. This was utilized by Russian engineers, who designed the E110 and E635 alloys, which are based on the Zr-Nb system with the addition of small amounts of Sn

and Fe in the case of the E635. These alloys have high strength and creep resistance. Due to its good corrosion resistance, the E110 was used as a fuel cladding. The E635 was used as a structural material because of its better mechanical stability. These alloys were relatively susceptible to oxidation and hydrogen uptake, which led to faster embrittlement.

To further optimize the properties of the E635 alloy, an alloy based on the system Zr-Sn-Nb-Fe called "ZIRLO" was designed in 1987. This alloy showed a lower corrosion rate at high temperatures, lower in-reactor corrosion rate, and higher creep resistance than Zircaloy-4. Due to its superior properties, it was used in almost all Westinghouse-designed plants in the United States and several European countries during the late 1990s [35].

One of the latest developments in zirconium alloys was the optimization of Zircaloy-4. It was shown that the reduction of the Sn content to 0.6-0.7 wt% in the Zircaloy-4 leads to an improvement of waterside corrosion resistance [36], which is one of the most critical properties for use in pressured water reactors. Cold working and thermal aging of the optimized Zircaloy was used to enhance the precipitation of Zr and Fe-based intermetallic particles, further increasing the corrosion resistance [37].

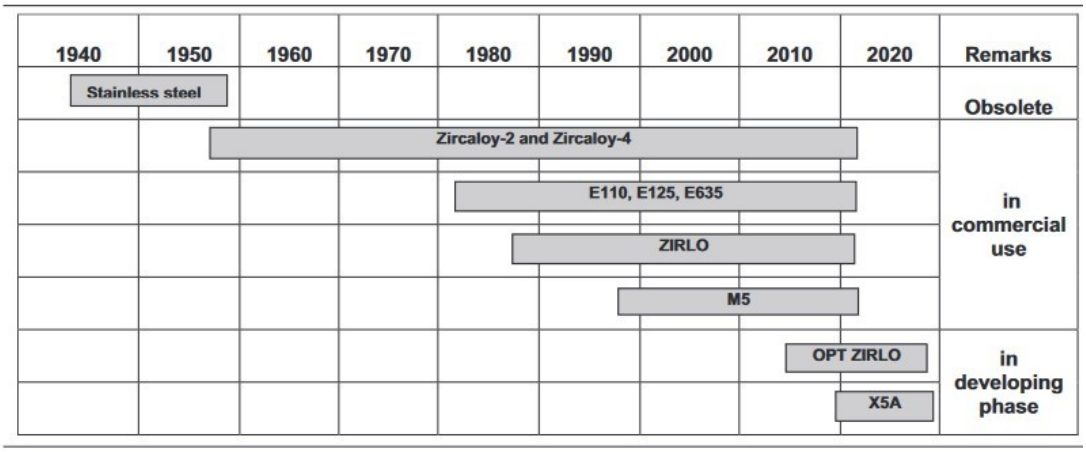

Figure 1.12 Timeline of nuclear cladding materials [27].

2 Aims of the thesis

Zirconium and its alloys are of high importance in the nuclear industry, where they are utilised as structural materials in fuel cladding due to their excellent mechanical properties and low cross section for thermal neutrons. Development of new improved alloys is a way to make nuclear energy safer and less expensive.

Two new zirconium alloys were developed with the aim to create highly strengthened alloy with $\alpha + \beta$ microstructure: Zr-4Sn-1Cr and Zr-4Nb-2Al. This work focuses on characterisation of these new alloys. It can be divided into two parts:

In the first section, we focused on understanding the phase transformations of the new alloys and investigating the microstructure to verify the presence of the intended $\alpha + \beta$ microstructure. The principal tasks can be summarised as follows:

- Verify the microstructure of the alloys using scanning electron microscopy.
- Study the phase transformations in situ using resistometry and differential scanning calorimetry.
- Determine the phase composition after annealing at different temperatures using x-ray diffraction and scanning electron microscopy.

The second part focuses on mechanical properties, which are strongly influenced by phase composition and microstructure. This section aims to determine the mechanical properties of the selected alloys after thermomechanical processing and explain the connection to their phase composition. The main tasks can be summarised as follows:

- Study the microhardness.
- Perform tensile tests on the alloys after thermomechanical treatment.
- Analyse the influence of phase composition on mechanical properties.

3 Studied material and experimental methods

3.1 Studied material

In this work, we characterize two zirconium alloys: Zr-4Sn-1Cr and Zr-4Nb-2Al (in wt%). These alloys contain one α stabilizing (Sn, Al) and one β stabilizing (Cr, Nb) element. In the first alloy, tin was added to promote solid solution hardening. Chromium was added with the aim to strengthen the material by precipitation of intermetallic phases and to stabilize the β phase. The second alloy contains a lower amount (2 wt%) of α stabilizing aluminum and a higher amount (4 wt%) of β stabilizing tin, with the goal to further stabilize the β phase.

The studied alloys were produced in ÚJP Praha by electric arc melting, during which elemental metals were melted by electric current and mixed to form the desired alloy. However, the materials fabricated by this process contain high amounts of defects. These defects are produced by non-ideal mixing and by different cooling rates in different parts of the material. To get rid of such defects, homogenization heat treatment was performed. The alloys were annealed at temperature of 1200 °C for 4 hours. This temperature was chosen to be sufficiently higher than the expected β transus, so that the homogenization treatment would be performed in the β phase field.

3.1.1 Hot swaged samples

To achieve grain refinement and $\alpha + \beta$ microstructure, we used hot rotary swaging as a thermomechanical treatment of the studied alloys. Due to dynamic recovery at increased temperatures, subjecting the material to substantial deformation without forming internal defects is possible. The hot swaging of Zr alloys is done in two steps, the first one is performed at temperatures above the β transus [6], [38]. Growth of large β grains is promoted during deformation at this temperature. During cooling from the temperatures above the β transus, the α phase grows from the large β grains. The resulting α phase is commonly lamellar with Widmanstätten microstructure. The second step is deformation in the $\alpha + \beta$ phase field. During this step, the coarsening of the α grains is promoted, resulting in small equiaxed α grains [6]. The temperature parameters chosen for the hot swaging of the alloys are discussed in detail in chapter 4.5.

In order to conduct the swaging, the material had to be prepared in the form of cylindrical rods. This was done in an arc furnace, where an electric arc melted the material in an argon atmosphere. This process resulted in rods that were 140 mm long and had a diameter of 12 mm. After the preparation of the rods, we performed the hot swaging. The rods were heated by an induction coil, which was positioned in front of the swaging machine. The temperature of the heated rod was monitored by an infrared camera. After the rod was heated to the desired temperature, it was manually fed through the swaging machine. The diameter of the rods was decreased by 0.25-0.5 mm in each subsequent passage through the machine. During the forging in the β region, the diameter of the rods was

reduced to 8 mm, followed by forging in the $\alpha + \beta$ region in which the diameter was further reduced to 5.5 mm.

3.2 Experimental methods

3.2.1 Scanning electron microscopy (SEM)

Scanning electron microscopy uses a beam of high-energy electrons to create an image of the studied surface. Electrons with energy usually between 10-30 keV are focused into a beam that scans the surface and produces a variety of signals. By detecting these signals, we can obtain information about the chemical composition, morphology, and crystal orientation of the sample. Due to the short de Broglie wavelength of high-energy electrons, it is possible to study objects smaller than 1 nm.

Firstly, a beam of electrons must be created, which is usually done using a tungsten filament or a field emission gun (FEG). In microscopes where tungsten filament is used, the electron beam is created by heating the filament to temperatures over 2500 °C. At this temperature, electrons are thermally emitted from the filament and further accelerated by electrical voltage. The field emission gun, also known as a cold cathode emitter, works on the principle of quantum tunneling caused by a strong electric field. In comparison with the tungsten filament, FEG creates a very stable, bright electron beam [39]. The electron beam is then collimated by magnetic condenser coils and scanned across the specimen by deflection coils (see figure 3.1). The electrons then penetrate the surface and interact with the electrons of the specimen. The interaction volume of the electron beam has a "pear" shape (see figure 3.2), and its size is determined by the energy of the beam, the chemical composition of the specimen, and the incidence angle of the beam. The interaction of the primary electron beam with the sample creates secondary electrons (SE), Auger electrons, backscattered electrons (BSE), and characteristic x-rays [40].

Each of these signals gives us different information about the specimen. The secondary electrons are electrons excited from the specimen by the primary beam. These electrons have low energies (below 50 eV) and can escape only from a near-surface layer of the material, providing information about the morphology of the surface. Backscattered electrons are electrons of the primary beam that are scattered through a large angle and re-emerge from the sample. Such scattered electrons have much larger energies and come from larger volumes than SE. The probability of scattering is proportional to the atomic mass of the scattering atom, which means that BSE gives us information about the chemical composition (chemical contrast). Depending on the orientation of the studied crystal, BSE can be channeled along particular crystallographic planes, leading to a contrast between different crystallographic orientations (channeling contrast) [40].

Characteristic X-rays are created when the inner shell electron of the material is excited out of the sample by a primary electron. This creates an empty energy level, which is soon filled by electrons from a higher energy orbit, which leads to the emission of x-rays of energy equal to the difference between the two levels. The structure of electron energy levels is unique for each element, and so the emitted X-ray is characteristic of a given element. The detection of the characteristic

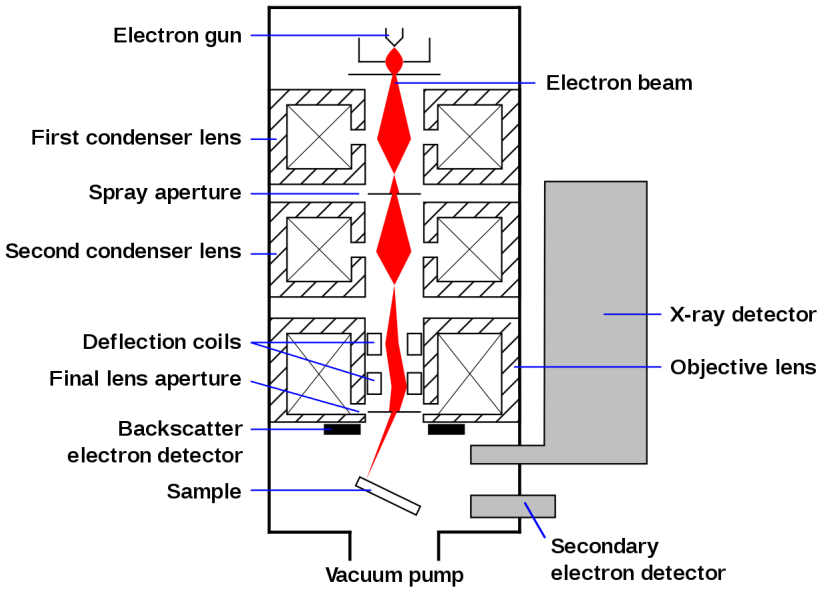

Figure 3.1 Diagram of scanning electron microscope [41].

X-rays is employed in energy-dispersive X-ray spectroscopy (EDX or EDS), which is used to determine the chemical composition [40].

As it was mentioned, the SEM image is constructed by detecting two types of electrons – backscattered electrons and secondary electrons. Traditionally, they are detected using one BSE detector and one SE detector. Newer microscopes employ multiple in-lens detectors to increase the amount of information gathered. These detectors collect both BSE and SE, and the detected electrons are later sorted by energy or emission angle. In this work, we used a detection system with three detectors to gather SEM images, as shown in figure 3.3. These detectors are placed along a tube that is under 8 kV voltage, which attracts the signal electrons. The first of the detectors is the T1, which detects the high-energy BSE and provides chemical and orientation contrast. Secondary electrons, which have a lower energy than BSE, are instead focused through a hole in the middle of the T1 and are registered by the T2 detector. This detector provides mainly morphological information. SE with even lower energy than 2 eV pass the T2 detector and are registered by the T3 detector. These electrons are th most surface-sensitive and provide information about small surface features. They are strongly affected by surface electric fields, providing surface charge contrast [43].

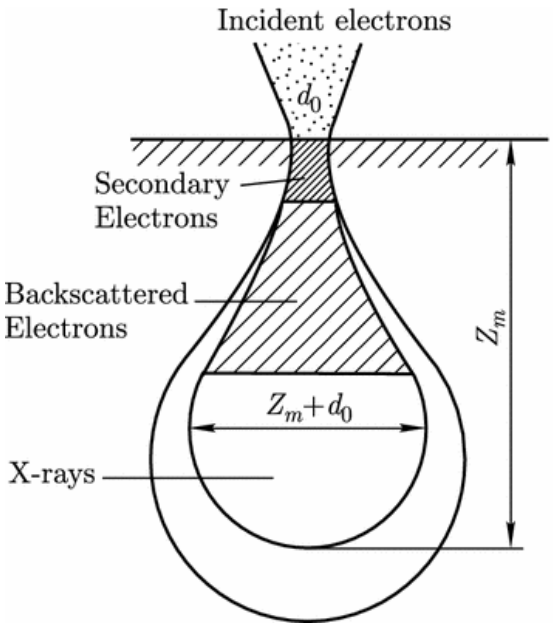

Figure 3.2 Interaction volume of primary electrons in SEM [42].

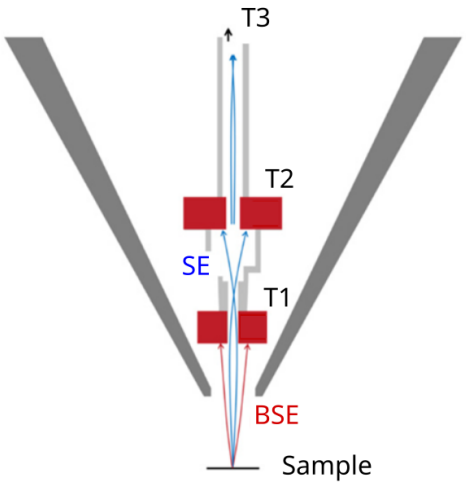

Figure 3.3 Diagram of detectors in SEM [43].

3.2.2 Energy dispersive spectroscopy (EDX)

Energy dispersive spectroscopy is an analytical method used for qualitative and quantitative chemical analysis of materials. EDX can identify elements heavier than beryllium and lighter than uranium. It works on the principle of detecting the energy of characteristic X-rays created by the interaction of the beam of primary electrons with the atoms in the material. We obtain an energy spectrum, which is then analyzed. Qualitative chemical analysis is done by identifying the characteristic lines of a given element with peaks in the measured energy spectrum. The abundance of a given element can be determined from the integrated intensity of its characteristic peaks.

The spatial resolution of EDX is determined by the volume that is penetrated by the electron beam. This volume is commonly called the "interaction volume for X-rays", its size depends on the energy and diameter of the electron beam and the composition of the analyzed material. Higher electron energy results in greater penetration depths and larger interaction volumes. Denser materials tend to have smaller interaction volumes due to increased scattering and absorption of the incident electrons [44].

To estimate the size of the interaction volume, we used the program Casino, which uses the Monte Carlo method to simulate the paths of individual electrons. The simulation was performed for both alloys and electron energies of 5, 10, and 30 keV. The results of electron trajectories for the alloy Zr-4Sn-1Cr are in figure 3.4. It is evident that the interaction volume rapidly increases with the electron energy. At 5 keV, almost all the electrons lose all their energy in a spherical volume with a diameter of 200 nm, while at 10 keV, the diameter increases to around 500 nm. At 30 keV, the volume in which the characteristic X-rays can be produced is much larger, with a diameter of around 2.5 μm. It is important to note that the number of produced X-rays is lower at the outer parts of the interaction volume because these electrons might not have sufficient energy to produce a characteristic X-ray [45].

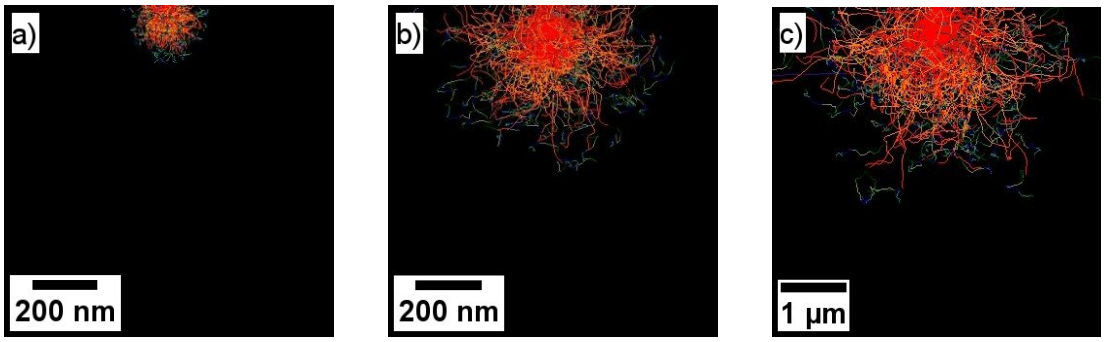

Figure 3.4 Simulated interaction volumes for Zr4Sn1Cr at energies a) 5 keV b) 10 keV and c) 30 keV.

3.2.3 SEM sample preparation

Samples for SEM observation were prepared by grinding on sandpapers of different grits from 320 to 4000, followed by final polishing. We used two different final polishing methods to prepare the surface. The first method was polishing on special cloth with a 1:3 volume ratio of 30% hydrogen peroxide and suspension of colloidal silica OP-S for 20 minutes. In the second method, we used the Buehler VibroMet 2. In this method, the samples were moved by vibrations on a cloth surface, which was submerged in an alumina suspension. The vibrational polishing was done in two steps, with the first polishing on 0.3 µm sized alumina particles and the second on 0.05 µm sized particles. Each of these steps was performed for a duration of 4 hours.

The first method (OP-S) led to insufficient polishing. The signal in both BSE and SE had a very weak contrast, and many of the details were not visible. In some cases, some contrast was visible, for example, between the intermetallic phase and the α phase in Zr-4Sn-1Cr (see figure 3.5a). This is due to the large difference between the composition of these two phases. The contrast between different grains was either not visible or weak, like in the case of Zr-4Nb-2Al, where despite that, different α lamellae could have been distinguished. This is very well visible in the figure 3.5a, where the α phase looks like one homogenous grain. The second method, vibrational polishing, gave more promising results. Unlike after the OPS, individual α grains were distinguishable (see figure 3.5b), but the signal was insufficient to see an orientational contrast between them.

After both polishing methods, the surface was damaged by zirconium hydride. During the polishing, the surface is in contact with the water or hydrogen peroxide present in the polishing suspension. Zirconium interacts with the oxygen present in the suspension, which then leads to the release of hydrogen into the material, forming zirconium hydrides [46]. The presence of hydrides on the surface is an issue because they obscure the actual microstructure of the bulk material. After the OPS polishing, the hydrides were present as darker patches distributed on the surface. Furthermore, some grains contained more zirconium hydride than others, which could be explained by the fact that the hydride prefers $(0001)_\alpha||(111)_{hydride}$ and $[11\bar{2}0]_\alpha||[110]_{hydride}$ orientations to the α during nucleation [47] [48]. In the vibrationally polished samples, the hydrides were mainly located between α grains but were also present on the grains. In the figure 3.5b they are visible as dark gray oblong regions in α grains.

To obtain information about the bulk microstructure of the alloys, we had to remove the zirconium hydrides without damaging the surface. This was done on the vibrationally polished samples by an ion beam milling system, Leica EM RES102, where the surface is bombarded by argon ions that remove a small layer of the surface. The ion milling was done in two steps; in the first step, the ions were directed onto the surface under the angle of 10°. The advantage of a higher angle is a higher material removal rate. However, it leads to the creation of surface topology. Such surface topology lowers the SEM signal because it increases the probability of absorption of the back-scattered and secondary electrons. A second step of milling at a lower angle of 4° was performed to mitigate the artificial topology.

We tried different durations of both ion milling steps to optimize the time and ensure that the resulting surface is rid of the hydride. Sufficient results were obtained after 3 hours of milling, followed by 1.5 hours of flattening the surface

at lower angles, after which large areas of the surface were suitable for SEM imaging. However, even after 3 hours, isolated regions of hydride were present on the surface, as shown in figure 3.5c. SEM images presented in section results and discussion (section 4) were prepared by vibrational polishing followed by ionic polishing.

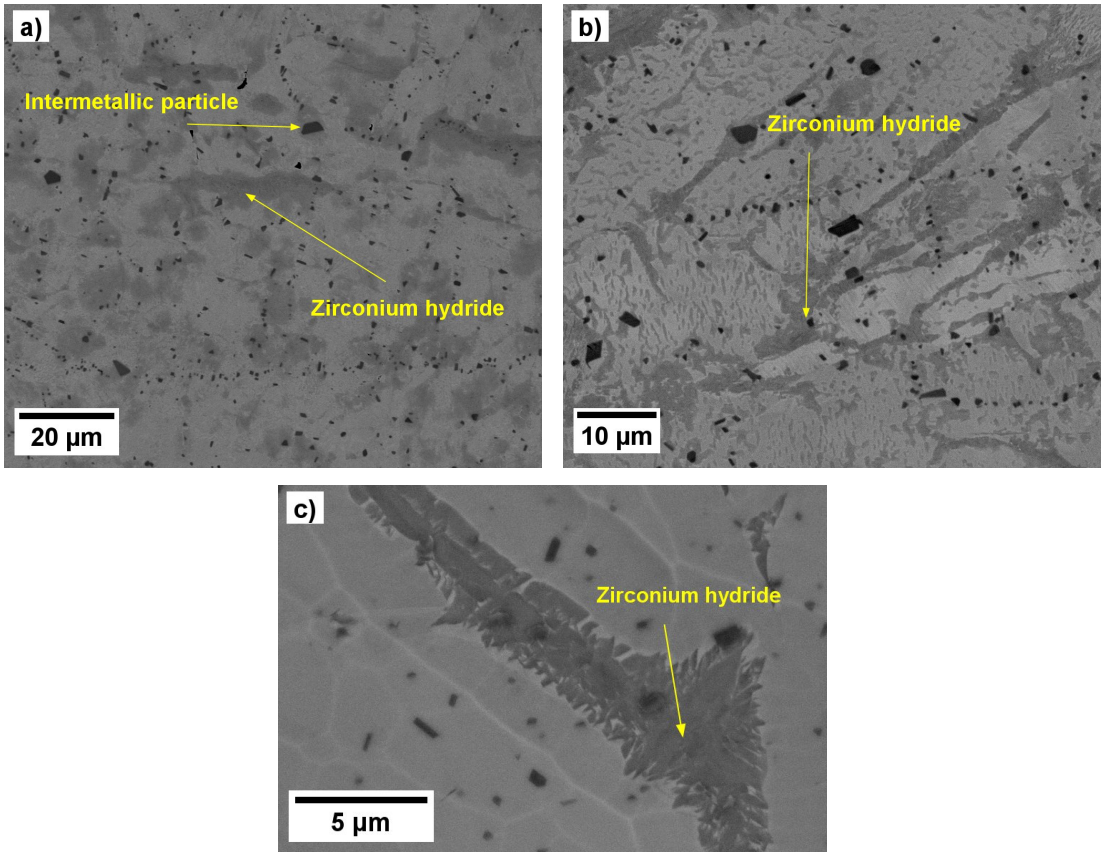

Figure 3.5 SEM image of zirconium hydride present in Zr4Sn1Cr after different polishing methods. a) OPS polishing. b) Vibrational polishing. c) Vibrational + ion polishing.

3.2.4 X-ray diffraction analysis (XRD)

X-ray diffraction is a technique for characterizing the structures of crystalline materials. It works on the principle of constructive interference of X-rays scattered by electrons in the studied sample. X-rays are produced by a cathode X-ray tube and later monochromatized, collimated, and directed towards the sample. The X-rays are scattered elastically by the atomic planes in the sample and produce constructive interference according to Bragg's law:

$$2d_{hkl} \sin\theta = n\lambda, \tag{3.1}$$

where d_{hkl} is the spacing of {hkl} planes generating the diffraction, θ is the diffraction angle, n is an integer and λ the wavelength of the X-rays.

In this work, we used the Rigaku R-axis RAPID II diffractometer. This diffractometer operates at a voltage of 50 keV and a current of 40 mA, producing Mo Kα X-ray radiation. The instrument also has a graphite monochromator,

which selects the Mo Kα_1 spectral line with the wavelength of 0.7093 Å. This diffractometer operates in a transmission geometry, where the diffracted x-rays penetrate the sample and are detected by a cylindrical 2D detector. The sample is located in a motorized goniometer, which tilts the sample along the horizontal axis ϕ and vertical axis ξ. This motion allows us to obtain diffraction from different crystal planes. The measurement results in a diffraction image (see figure 3.6) obtained by the 2D detector. The image is then azimuthally integrated to obtain the conventional diffraction line profile [49].

We prepared the samples for XRD using SiC sandpapers to achieve thickness between 100-150µm. This thickness was chosen as a compromise between minimal absorption and maximal diffracting volume. The fitting of the line profiles was performed using the program X'Pert HighScore Plus.

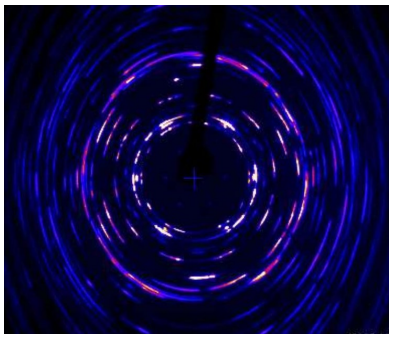

Figure 3.6 XRD image captured by 2D detector.

3.2.5 Differential scanning calorimetry (DSC)

Differential scanning calorimetry is a thermoanalytical technique commonly used to study phase transformations. In this work, we used the Netzsch DSC 404 C Pegasus DSC device, which measures heat-flux DSC. In this method, the sample and a reference are connected by a heat bridge and subjected to a constant heating rate. The measured signal is a temperature difference between the sample and the reference, usually plotted as a function of temperature or time.

When a first-order transition occurs in the measured sample, the release or absorption of heat results in the change in temperature difference between the sample and the inert reference. This change in temperature difference is then detected as a peak in the DSC signal. Based on the orientation of the peak, we can determine if the process is exothermic or endothermic. If an exothermic process occurs in the material, we detect an increase in sample temperature compared to the reference. In case of an endothermic effect, the sample temperature increase slows down or stays constant. The start and end of a first-order transition are characterized by the onset and endset of the measured peak, respectively.

Second-order transitions are characterized by an abrupt change in the heat capacity and are detected as a rapid change in the baseline of the DSC signal.

We performed the DSC measurements in situ during heating up to 950 °C and cooling from 950 °C to room temperature, in both cases at a rate of 5 °C/min. Samples for this method were cut by Accutom-50 precision saw into cubes of an approximate weight of 50 mg. The samples were subsequently polished using sandpapers of 1200 grit to remove any impurities from the surface caused by the cutting.

3.2.6 Electric resistance measurements

Electric resistance measurements provide information about the processes that take place in the material. Precipitates, grain boundaries, and phase boundaries disrupt the periodicity of the electronic potential, leading to the scattering of conduction electrons and an increase in electric resistance. Any change in the material structure, for example precipitation of a second phase, is accompanied by a change in electric resistance. Therefore, electric resistance measurements may be employed to study microstructural and phase transformations in situ.

In this work, we measured the resistance using the four-point method. The diagram and the sample used for this method are shown in figure 3.7. An electric current I is passed through two outer contacts (contacts 1 and 4 in figure 3.7), while the voltage is measured between the inner contacts (contacts 2 and 3 in figure 3.7). In this arrangement, the resistance of contacts 1 and 4 do not affect the measurement. the resistance of the voltmeter contacts 2 and 3 can be neglected since the resistance of the voltmeter is much greater than the resistance of the sample. Other errors affecting the measurement are transient and thermoelectric effects at the voltage contacts. These effects change the measured voltage due to temperature and material differences between the contacts and the sample material. These effects are eliminated by commutating the current and averaging the measured voltage. the measured electric resistance R is then calculated as:

$$R = \frac{U}{I}, \tag{3.2}$$

where U is the averaged voltage, and I is the absolute value of current passing through the sample.

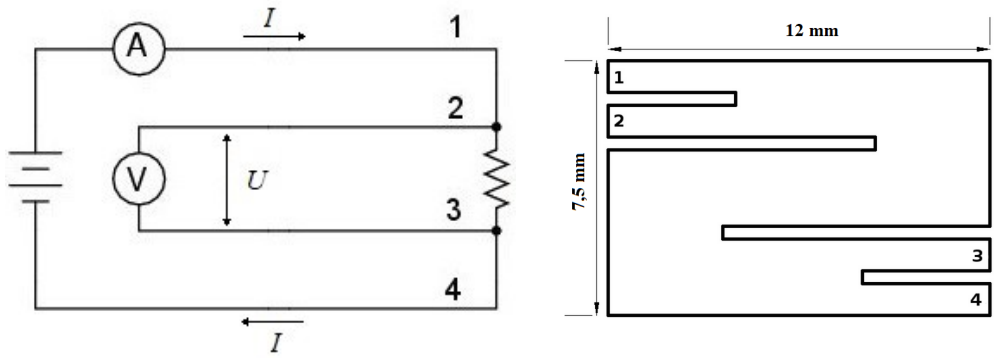

Figure 3.7 Diagram of the four-point electric resistance measurement and the sample used for this method.

In this work, we performed four-point resistance measurements in situ during heating. The sample was prepared according to the diagram in figure 3.7 and polished with sandpapers of grit up to 1200 to remove any impurities from the surface. Next, the sample was positioned in a furnace with a protective argon atmosphere and heated up to 900 °C at a rate of 5 °C/min. The current was supplied by Sourcemeter Keithley 2420, and the voltage was measured by Nanovoltmeter Keithley 2182.

3.2.7 Micro hardness testing

The indentation test is a standard method to characterize the material properties. It is used to measure the hardness of the material, but it can also provide information about other properties, such as stiffness and yield strength. In this work, we performed the microhardness tests on the indentation device Qness Q10. We used the Vickers indentation method, in which a square base pyramid-shaped diamond indentor is pressed into the surface of the material. The Vickers microhardness (HV) is then given by the ratio of the force applied by the indentor to the surface area of the resulting indentation. Due to the geometry of the pyramidal indentor, the value of HV is calculated by the equation:

$$HV = \frac{2\sin(136°/2)F}{d^2} \approx \frac{1.8554F}{d^2}, \tag{3.3}$$

where the F is the applied force, which in the case of this work corresponded to a weight of 0.5 kg, d is the average diagonal length of the indentation, and 1.8554 is a factor given by the pyramidal geometry [50].

In this work, the microhardness tests were performed on the samples prepared by vibrational and ion polishing used for SEM imaging.

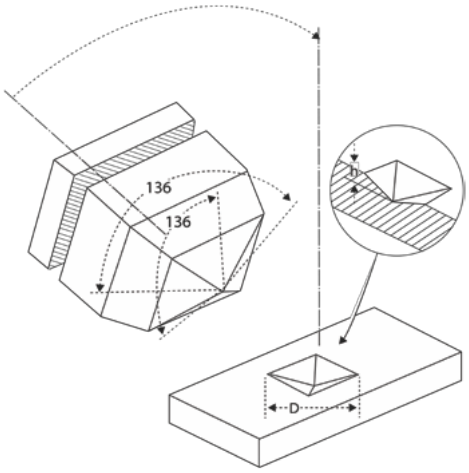

Figure 3.8 Diagram of the Vickers hardness measurement [51].

3.2.8 Tensile testing

Tensile tests are commonly performed to obtain mechanical properties of materials such as strength, toughness, and ductility. During the test, the specimen was subjected to uniaxial tension until failure. The specimen was gripped by one arm that remained static and a second arm that deformed the sample at a constant speed. We performed the tests on the Instron 5582 machine at a strain rate of 10^{-3}/s. The sample geometry used for tensile testing is shown in figure 3.9. It had enlarged ends of cylindrical shape, which were used to grip the specimen during testing. The gage section was cylindrical with a length 10 mm and a diameter of 2 mm.

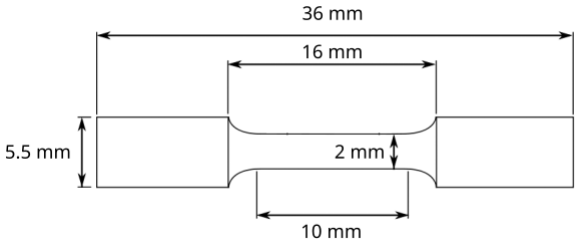

Figure 3.9 Geometry of tensile test specimen.

During loading, we obtain the relation between engineering stress and engineering strain, which can be plotted as a stress-strain curve. The engineering stress,

$$\sigma_e = F/A_0, \tag{3.4}$$

is defined as the tensile force F applied to the initial cross-section area A_0. And the engineering strain,

$$\varepsilon_e = \Delta L/L_0, \tag{3.5}$$

is defined as the change in length ΔL divided by the initial length L_0. When a material is subjected to small stresses, the bonds between atoms are stretched. Such deformation is reversible, and when the stress is removed, the material returns to its original length. This is called elastic deformation and is observed as a linear dependence of the stress-strain curve. The elastic deformation is characterized by Young's modulus E, which is defined as

$$E = \sigma_e/\varepsilon_e. \tag{3.6}$$

When the stress increases above a certain point, the deformation ceases to be completely reversible, and we speak of plastic deformation. This deformation is no longer caused by the stretching of bonds but rather by the motion of dislocations, twinning, and phase transformations, such as martensite formation. Usually, the start of plastic deformation is visible as a deviation from linearity in the stress-strain dependence. The offset yield strength $\sigma_{0.2}$ is the limit that characterizes the start of plastic deformation. It is obtained by constructing a linear line parallel to the elastic stress-strain plot with an offset of 0.2%. The $\sigma_{0.2}$ offset yield strength is then the stress at which this line intersects the stress-strain curve.

The ultimate tensile strength is defined as the highest value of engineering stress. Up to this point, the deformation of the specimen should be uniform in the measured length. In ductile materials, the tensile strength is the point at which the deformation starts to localize. This leads to the formation of a neck, which is observed as a decrease in the stress-strain curve. Brittle materials fracture before any neck can form, and the tensile strength is the fracture strength.

The ductility of a material is the maximal plastic deformation before fracture. In most ductile materials, the elastic deformation at fracture is relatively small compared to the plastic deformation and can be neglected. In such case, the ductility is defined as

$$\%El = \frac{L_f - L_0}{L_0}, \tag{3.7}$$

where the L_f is the length at fracture.

It is desirable to obtain data that can be used to characterize the material properties under different loading conditions. In that case, the data needs to be presented in terms of true stress and true strain. True stress is defined as

$$\sigma = F/A, \tag{3.8}$$

where A is the cross-section area at the time of the applied force. The true stain is defined as

$$\epsilon = \ln(L/L_0). \tag{3.9}$$

If the deformation is uniform along the whole gage length, the true quantities can be calculated from the engineering ones as

$$\sigma = \sigma_e(1 + \varepsilon_e) \tag{3.10}$$

$$\epsilon = \ln(1 + \varepsilon_e). \tag{3.11}$$

4 Results and discussion

4.1 Characterisation of initial state of Zr-4Sn-1Cr

4.1.1 X-ray diffraction

We investigated the phase composition of the initial state of Zr-4Sn-1Cr using x-ray diffraction in transmission geometry as described in section 3.2.4. The measured XRD line profile, shown in figure 4.1, was fitted with the theoretical models of hcp and Laves C15 structures. The theoretical positions and relative intensities of the peaks are shown in the lower part of the figure 4.1. The analysis concluded that the alloy consists of the hcp α phase and the intermetallic Laves C15 $ZrCr_2$ phase.

From the area of the peaks, we determined that the majority (97.3 wt%) of the material consists of the α phase, and the remaining material (2.7 wt%) crystallized in the Laves C15 phase. However, the determined fraction should be taken only as an approximative value because of the local nature of the measurement. The integrated intensity of the peaks corresponds to the local composition of a relatively small interaction volume (the x-ray beam had a width of 0.3 mm, and the sample thickness was approximately 100 μm), which can differ from the average phase composition in the whole material. From the position of diffraction peaks, we determined the lattice constants. For the hexagonal α phase the lattice parameters $a_\alpha = 3.223\,\text{Å}$, $c_\alpha = 5.150\,\text{Å}$ were found. For the cubic Laves phase $a_{ZrCr2} = 7.226\,\text{Å}$ was determined. The weight fractions and lattice parameters of α and $ZrCr_2$ phases in the initial state of Zr-4Sn-1Cr alloy are given in table 4.1.

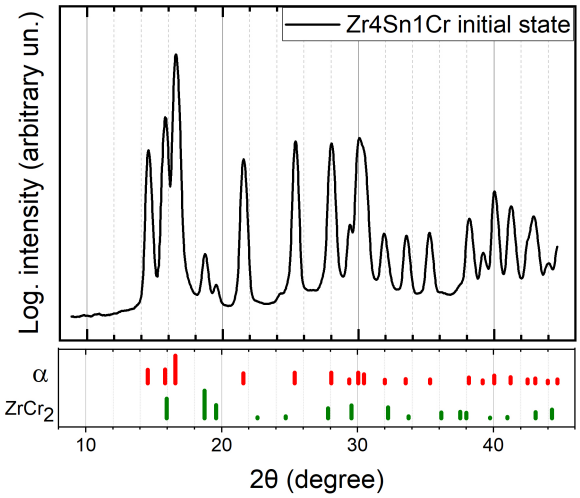

Figure 4.1 XRD profile of the initial state of Zr-4Sn-1Cr. The positions of peaks belonging to α phase and ZrCr2 are indicated in the lower part of the image by red and green markers, respectively. The length of the markers corresponds to the theoretical intensity of the peaks.

Phase	Weight fraction (%)	a (Å)	b (Å)	c (Å)
α	97.3	3.223	3.223	5.150
$ZrCr_2$	2.7	7.226	7.226	7.226

Table 4.1 Weight fractions and lattice parameters of phases present in Zr-4Sn-1Cr.

4.1.2 SEM and EDX

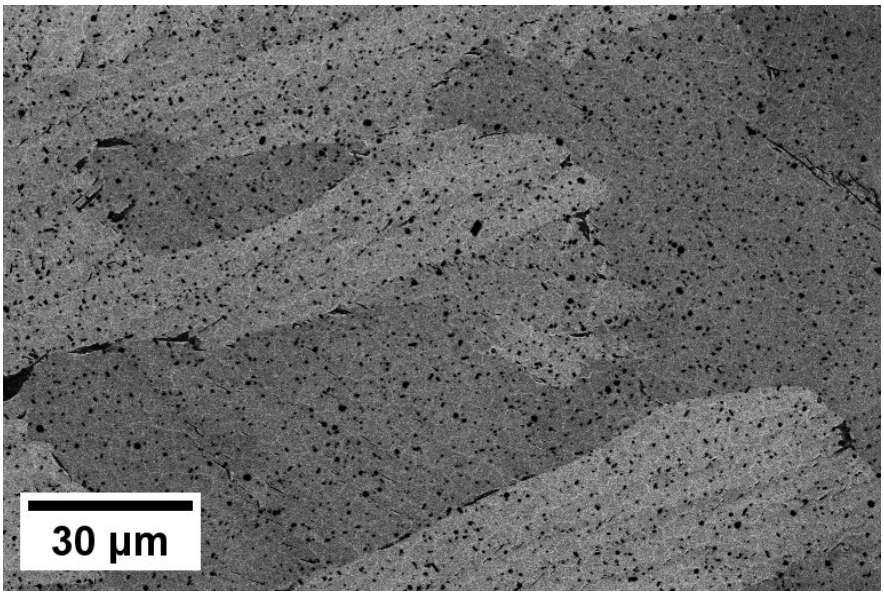

Figure 4.2 SEM photograph of the microstructure of Zr-4Sn-1Cr (BSE contrast).

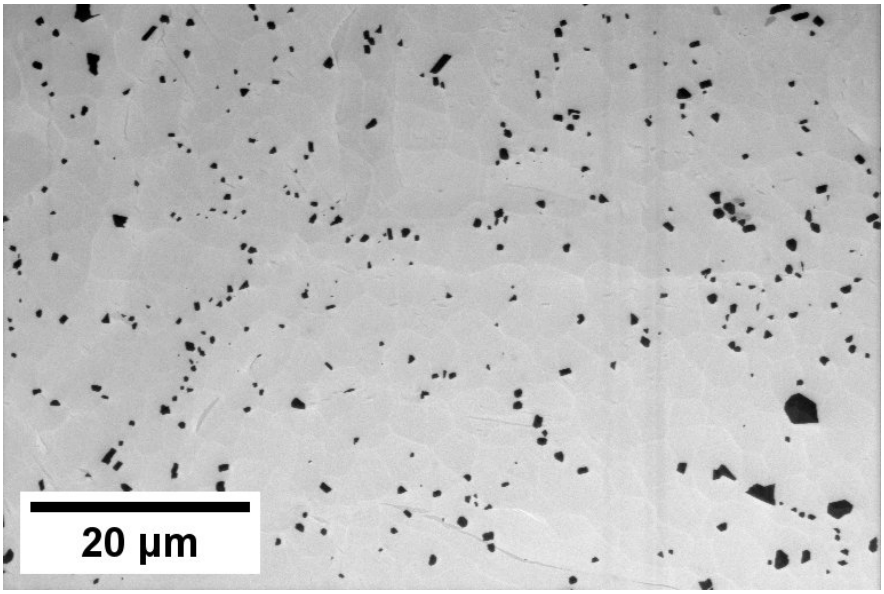

Figure 4.3 SEM photograph of $ZrCr_2$ crystals (low energy SE contrast).

We used scanning electron microscopy to observe the microstructure of the initial state. We used mainly the BSE detector, which gives chemical and channeling contrast, and the low energy SE detector, which collects secondary electrons only

from the nearest surface. In figure 4.2, which was captured using the BSE detector, we see large α grains. We can also observe chanelling contrast between differently oriented grains. Smaller black dots are the Laves C15 particles, which are visible due to the chemical contrast between the α grains and the Laves C15 phase.

Figure 4.3 captured using low energy secondary electrons provides a better view of the $ZrCr_2$ particles. The distribution of these particles is not homogeneous, and their precipitation seems to be preferred at specific nucleation centers. Such centers could have been the β grain boundaries, which were present in the material during homogenization at temperatures above the β transus. We determined that the crystals have apparent diameters up to 3.5 µm.

We performed the EDX chemical composition measurement on the α and $ZrCr_2$ phases. The used voltage was 10 keV, for which we in chapter 3.2.2 calculated the radius of interaction volume to be around 500 nm. The particles of the Laves phase in figure 4.4 (location 1) contain 63.5 at. % of chromium and 36.5 at.% of zirconium. That is in accordance with the Zr-Cr phase diagram in figure 1.7 and the approximate 1:2 stoichiometric ratio. The measurements from the α phase at locations 2 and 3 in figure 4.4 show that all chromium in the material is incorporated in the intermetallic crystals and α phase is a solid solution of only zirconium (95.5 wt%) and α stabilizing tin (4.5 wt%). The results of the EDX chemical analysis are in table 4.2.

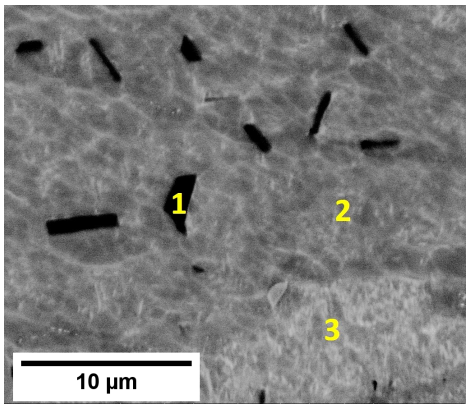

Figure 4.4 BSE image of the EDX measurement.

Location	Element	Wt %	At. %
1 ($ZrCr_2$)	Zr	50.2	36.5
	Cr	49.8	63.5
	Sn	0	0
2 (α)	Zr	95.5	96.5
	Cr	0	0
	Sn	4.5	3.5
3 (α)	Zr	95.5	96.5
	Cr	0	0
	Sn	4.5	3.5

Table 4.2 Weight fraction and lattice parameters of phases present in the initial state of Zr-4Sn-1Cr.

4.1.3 Conclusion to initial state characterisation

In this section, we investigated the phase composition and microstructure of the Zr-4Sn-1Cr alloy. We determined that the Zr-4Sn-1Cr consists of relatively large α grains and smaller intermetallic particles of $ZrCr_2$. The β phase was not detected in the alloy, which we attributed to the fact that all the β stabilizing chromium was retained in the intermetallic phase. We determined the lattice parameters and weight fractions of the phases by XRD and their chemical composition by EDX.

4.2 Temperature evolution of phase composition in Zr-4Sn-1Cr

A common means of the thermomechanical treatment of zirconium alloys is hot forging. This process consists of forging in the β and later in the $\alpha + \beta$ field [52], [38]. In this chapter, we investigate the $\alpha \rightarrow \beta$ transformation and other transformations that occur in the Zr-4Sn-1Cr alloy. The aim is to use this information later to correctly choose the parameters of the hot forging.

First, the sample in the initial state (described in previous chapter 4.1) was subjected to in-situ differential scanning calorimetry and electric resistance measurements during heating. The purpose of these measurements was to determine the temperature range where the $\alpha \rightarrow \beta$ transformation takes place, as well as to hint at other temperatures of interest where different changes in the alloy may occur. After that, we heat-treated the alloy at temperatures chosen based on these results and studied the samples by X-ray diffraction and scanning electron microscopy.

4.2.1 DSC and electric resistance measurements

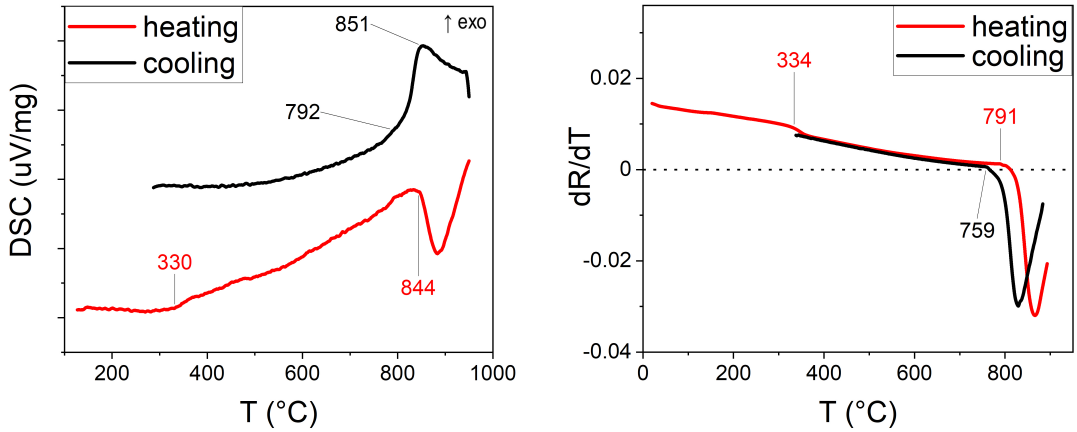

Figure 4.5 DSC and electric resistance measurements of Zr-4Sn-1Cr.

We performed the DSC measurement during heating and cooling in the temperature range 20-950 °C with a heating rate of 5 °C per minute. The result of the measurement can be seen in figure 4.5. In the graph, we omitted the start of heating and the end of cooling. The electric resistance measurement was executed in a similar way, with a heating rate of 5 °C per minute. The difference was that the maximum temperature was only 900 °C, which was due to the limitations of used equipment. To better understand the changes occurring in the material, it is more convenient to study the rate at which the resistivity changes rather than its absolute values. For this reason, the results in figure 4.5 are presented as the first derivative of resistivity with respect to temperature.

As expected, the $\alpha \rightarrow \beta$ transformation was detected in both DSC and resistivity measurements. Because of high α stabilization by Sn, the $\alpha \rightarrow \beta$ transformation is shifted to higher temperatures in comparison with unalloyed zirconium. From the DSC measurement during heating, we determined from

the onset of the peak that the start of the transformation is at 844 °C. Even though the end of the transformation is not visible in the measurement, we can see the maximum of the signal at 880 °C followed by returning of the signal towards the baseline, which indicates the slowdown of the transformation. Therefore, we can assume that the β transus is not far beyond the temperature of 950 °C. When analyzing the DSC signal, it is important to keep in mind that the kinetics of the transformation play an important role. This can be seen in the DSC signal during cooling, where the transformation is shifted to lower temperatures.

In the resistance measurement, the $\alpha \rightarrow \beta$ transformation is marked by a rapid decrease in resistivity. During heating, we can clearly see the change from a steady to a rapid decrease of dR/dT starting at 791 °C. This means that in the first part of the experiment, the resistivity of the sample was increasing steadily, and then the increase of resistivity slowed due to the $\alpha \rightarrow \beta$ transformation. As in the case of DSC, the end of the transformation was not detected because of an even lower maximum achievable temperature. During cooling, we can see the end of $\alpha \rightarrow \beta$ at 759 °C.

In both DSC and resistometry, a signal change was detected at around 330 °C. In the DSC during heating, this effect appeared as an increase in signal from the initial baseline. We detected no change at this temperature during the cooling experiment. In resistivity measurement during heating, a slight decrease in otherwise increasing resistivity was detected at around 334 °C.

4.2.2 XRD

From the results of DSC and resistivity measurements, we chose temperatures at which the Zr-4Sn-1Cr alloy was heat treated: 500, 700, 820 and 940 °C. We chose temperatures 500 °C and 700 °C to understand the changes that happen in the alloy when heated through the effect observed around 300 °C. The temperatures 820 °C and 900 °C were chosen to study the start and end of the $\alpha \rightarrow \beta$ transformation, respectively. The heat treatment was performed in the following way: the alloy was linearly heated at rate of 5 °C to the given temperature. We heat-treated the alloy at the temperature for 1 hour and then quenched the sample to suppress diffusion and at least partly preserve its high-

After each heat treatment, we performed X-ray diffraction measurement. The measured XRD profiles are in figure 4.6. We can see that at all of the selected temperatures (500-940 °C), the intermetallic $ZrCr_2$ is present in the alloy. We can see two intense reflections at 18.7 ° and 19.5° belonging to the (311) and (222) crystallographic planes of the cubic C15 Laves structure. Another intense peak at 16° corresponding to the (220) reflection of the Laves phase is overlapped by the strong diffraction of the (002) and (101) planes of α phase.

We can also see that the XRD spectrum lacks any strong diffraction peaks from the bcc β, even though from the DSC and resistometry, it is evident that α starts to transform into β at around 800 °C. The β phase is not present in the material because of the martensitic transformation that occurs when the β phase is subjected to rapid cooling. The temperature of the start and end of this transformation is mainly governed by the chemical composition of the β phase. We already determined that nearly all of the β stabilizing Cr is contained in the intermetallic particles. The lack of β stabilizing elements means that the martensitic start and

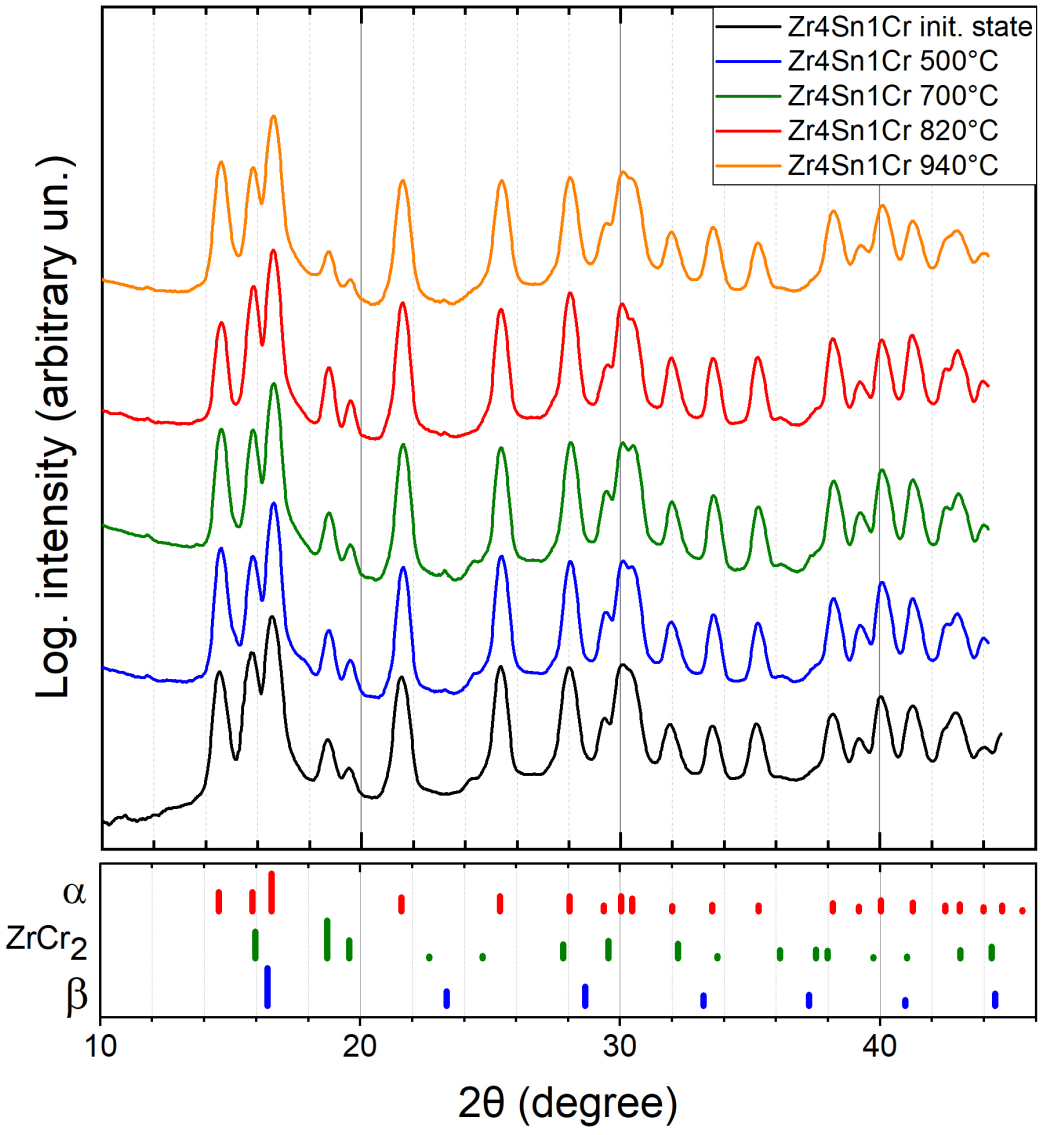

Figure 4.6 XRD profiles of the initial and heat-treated states of Zr-4Sn-1Cr.

end temperature is relatively high, and after quenching, all of the β is transformed to the hcp α' martensite. Because both the equilibrium α and martensitic α' have both hcp structure with relatively similar compositions, their diffraction patterns overlap.

4.2.3 SEM

In this section, we focus mainly on the evolution of the intermetallic phase $ZrCr_2$, which was determined to be present in the alloy in the temperature range up to 940 °C. In the initial state, we observed large particles of $ZrCr_2$ with diameters of their intersections up to a few μm (see figure 4.7a) that were heterogeneously distributed in the material, which sometimes formed chains of particles.

The $ZrCr_2$ particles significantly evolved when the sample was heat treated at 500 °C. In figure 4.7b, we see an SEM image of the sample taken using the back-scattered electrons. We can see small $ZrCr_2$ particles filling the α grains. These particles can be seen as dots or lines, indicating that they are fiber-shaped. We did not observe any change in the microstructure or size of the α grains after the heat treatment at 500 °C.

In the heat-treated sample at 700 °C, the intermetallic particles evolved in the same way as during the 500 °C treatment. The material contained the fiber-shaped $ZrCr_2$ particle, which filled the α grains (see figure 4.7c).

After the heat treatment at 820 °C, the sample contained intermetallic particles similar to the initial state (see figure 4.7d). In the figure, we can also see gray patches of zirconium hydride, which were present on the surface even after 3 hours of ion milling.

In the sample heat-treated at 940 °C, almost all of the original α phase transformed. In the figure 4.7e, we see martensitic plates that formed when the β was quenched. In some locations, we observed the original α grains, which indicates that the temperature of the β transus was not crossed.

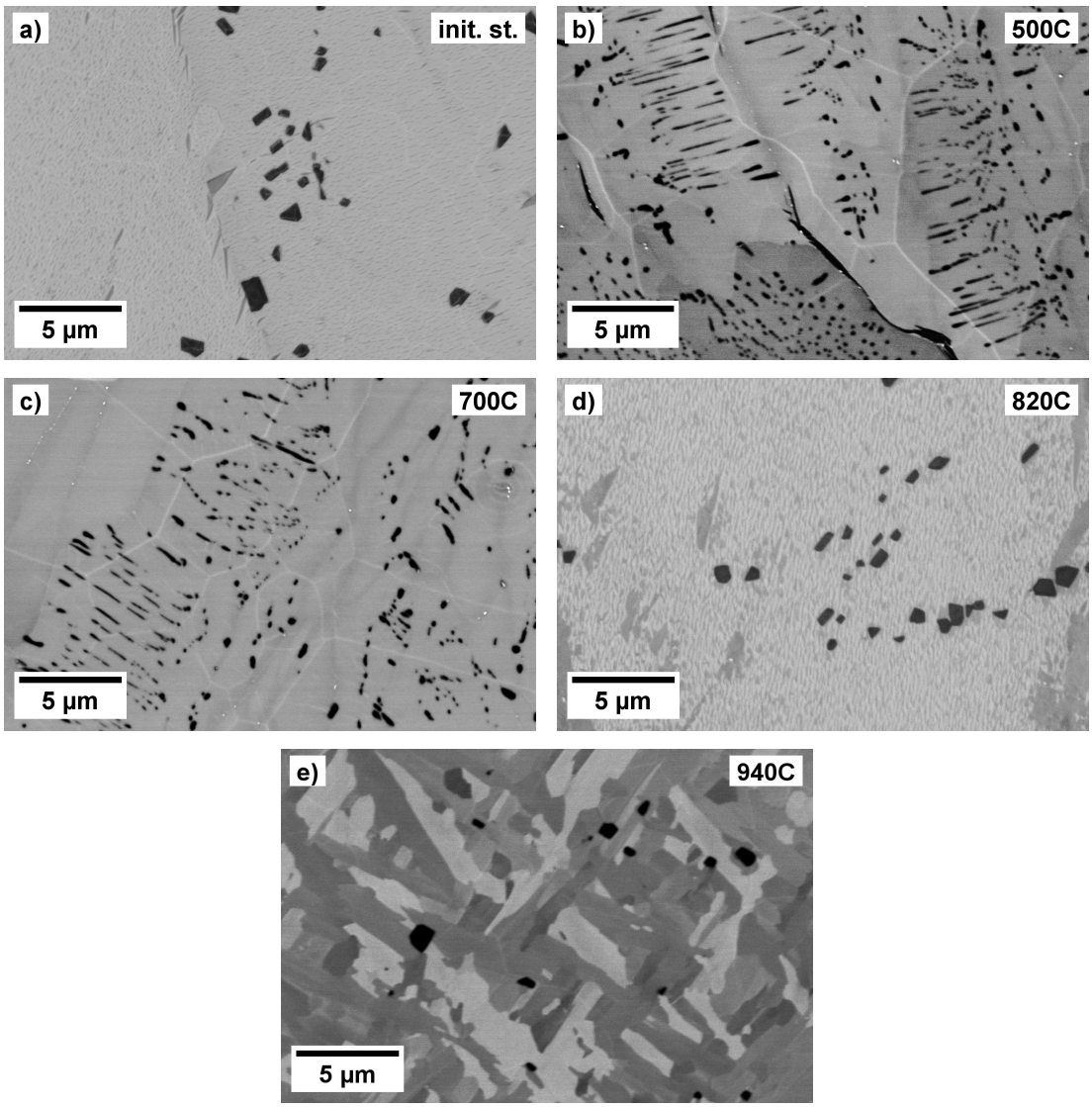

Figure 4.7 BSE images of $ZrCr_2$ particles in the Zr-4Sn-1Cr alloy a) in the initial state, b-e) after different heat treatments.

4.2.4 Discussion of phase composition evolution

In the SEM and XRD experiment, we observed the intermetallic $ZrCr_2$ phase present in the Zr-4Sn-1Cr alloy. We determined that the particles of $ZrCr_2$ were present after all heat treatments (500-940 °C) and observed changes in their microstructure after heat treatments at 500 °C and 700 °C. We observed the formation of α‘ martensitic plates after heat treatment at 940 °C and subsequent quench.

We calculated lattice parameters (see figure 4.8) and phase composition (see figure 4.9) from the XRD line profiles (figure 4.6) after each heat treatment. We measured no significant deviation of lattice parameters of both phases from those determined in chapter 4.1.1 (table 4.1). It was expected in the case of $ZrCr_2$ since it has a strict stoichiometric composition due to its ordered nature. We measured a stable fraction of $ZrCr_2$ after each heat treatment, around 2-3 wt%, which is within the expected error caused by the fitting of the XRD profiles and the local phase composition.

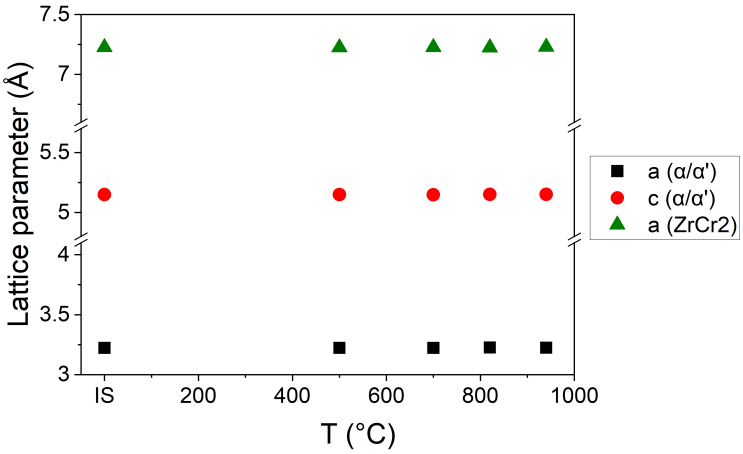

Figure 4.8 Lattice parameters obtained by XRD analysis of phases present in Zr-4Sn-1Cr after different heat treatments.

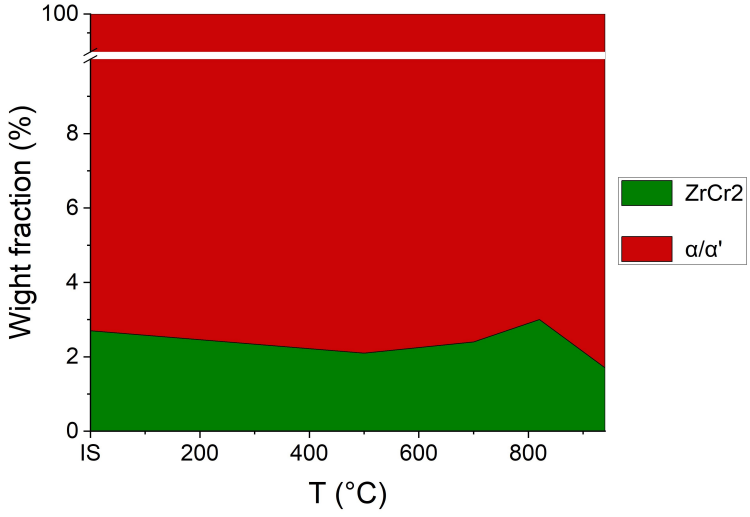

Figure 4.9 Phase composition of Zr-4Sn-1Cr after different heat treatments.

4.3 Characterisation of initial state of Zr-4Nb-2Al

The second investigated alloy, Zr-4Nb-2Al, differs from the first alloy in the ratio of α and β stabilizing elements. This alloy contains more β stabilising elements, 4 wt% of niobium instead of 1% wt chromium. Furthermore, niobium is more efficient in β stabilization, as discussed in chapter 1.3.3 (see the Zr-Nb phase diagram 1.9) At 620 °C and 18.5 at.% of Nb there is the eutectoid transformation $\beta \rightarrow \alpha + \beta$, meaning that below the temperature of 620 °C the $\alpha + \beta$ coexist in thermodynamic equilibrium [53]. At this temperature only 0.6 at.% Nb is sufficient for small fraction of β to exist in an equilibrium. The niobium content needed for the coexistence of α and β even decreases for lower temperatures. Compared with the Zr-Cr system, in which the temperature must be at least 836°C for equilibrium β to exist. Thus, we expected stronger β stabilization, which would result in the presence of the bcc β phase in the initial state.

4.3.1 X-ray diffraction

As expected, the XRD analysis detected both the α and β phases. Figure 4.10 shows the measured profile with the identified peaks. We determined that 87 wt% of the material crystallizes in the α phase, with the rest 13 wt% being the β phase. We also measured the lattice parameters for both phases, see table 4.3. We determined the lattice parameters $a_\alpha = 3.204\,\text{Å}$ $c_\alpha = 5.113\,\text{Å}$ for the α phase. For the β phase we determined the lattice parameter $a_\beta = 3.505\,\text{Å}$.

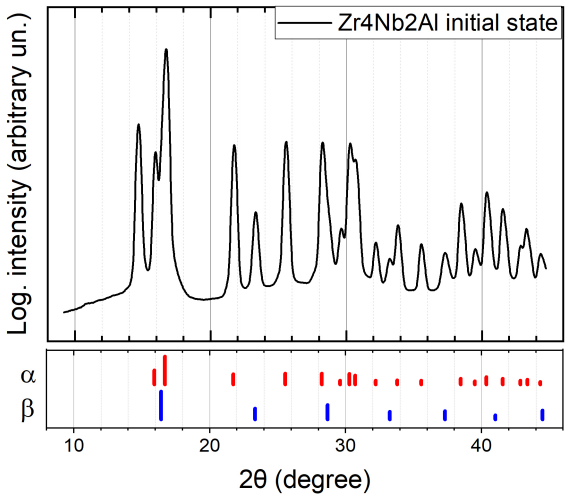

Figure 4.10 XRD profile of the initial state of Zr-4Nb-2Al.

Phase	Weight fraction (%)	a (Å)	b (Å)	c (Å)
α	87	3.204	3.204	5.113
β	13	3.505	3.505	3.505

Table 4.3 Weight fraction and lattice parameters of phases present in the initial state of Zr-4Nb-2Al.

4.3.2 SEM and EDX

We investigated the microstructure of the initial state of Zr-4Nb-2Al using scanning electron microscopy. As with the Zr-4Sn-1Cr alloy, we obtained most of the information about the material using the BSE and low-energy SE detectors. An overview of the microstructure is in figure 4.11, where we can see the chemical contrast between darker α and brighter β, meaning that the β phase contains heavier elements. This is in agreement with the assumption that the α phase would contain higher amounts of α stabilizing Al, which has atomic number 13 and is relatively light. On the other hand, the β phase contains β stabilizing Nb, which has atomic number 41. Note that zirconium, with its atomic number 40, lies next to Nb in the periodic table of elements

At first glance, we can see the difference in the microstructure when compared to the previous alloy. The microstructure consists of very fine α lamellae, which are surrounded by the β phase. This microstructure is typical for $\alpha + \beta$ zirconium alloys and forms when the α precipitates from the β phase during cooling. This results in the formation of α plates, which have a specific orientation with respect to the parent β phase [11]. Figure 4.12a presents a closer look at the microstructure. It is apparent that the α forms a much finer structure than in the Zr-4Sn-1Cr alloy. In the Zr-4Nb-2Al, the apparent width of the α laths is in the order of 1-2 µm. On the other hand, large α grains with the size in the order of tens of µm were observed in Zr-4Sn-1Cr. Interesting to note is the high contrast between α and β from low energy secondary electrons in figure 4.12b. In figures 4.12a and 4.12b, we can also see the light polyhedral-shaped contours that arise from the surface morphology created during ion polishing.

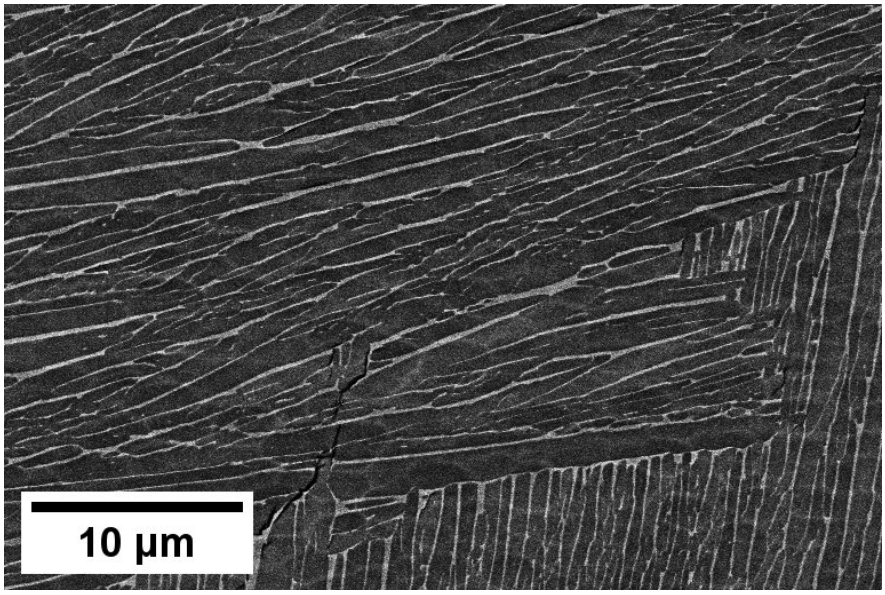

Figure 4.11 BSE image of the initial state Zr-4Nb-2Al.

We investigated the composition of the α and β by the EDX analysis. The energy of characteristic X-rays is similar for Zr and Nb due to their proximity in the periodic table. The Zr Lα line with the energy of 2.044 keV overlaps with the Nb Lα line with the energy of 2.169 keV. This problem is usually solved by EDX analysis from their Kα lines, which can be distinguished. To excite

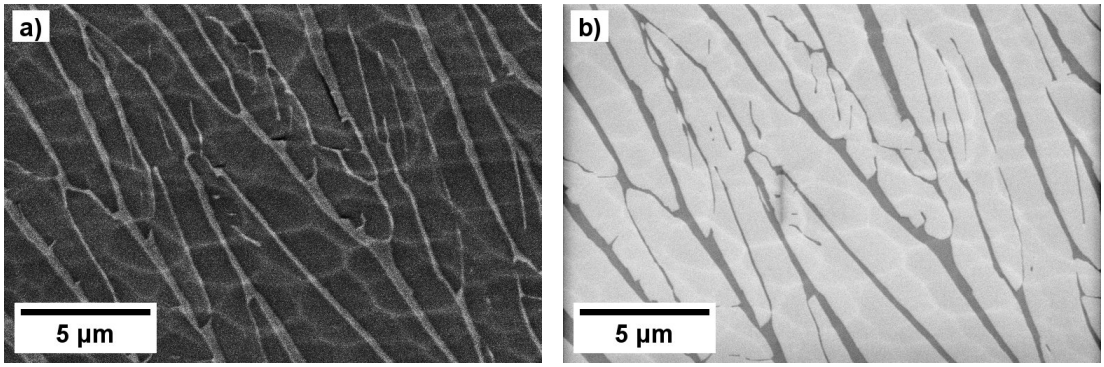

Figure 4.12 SEM image of the initial state Zr-4Nb-2Al. a) BSE contrast, b) low energy SE contrast.

Scan	Phase	Zr (wt%)	Nb (wt%)	Al (wt%)
1	α	98	0	2
	β	83	16	1
2	α	97	1	2

Table 4.4 Results of quantitative EDX analysis of the initial state of Zr-4Nb-2Al.

these spectral lines, it is advised to use an electron beam of an energy that is at least double the energy of the spectral lines, which means 30 keV in this case. However, at this energy, we calculated that the interaction volume from which the x-rays are collected is around 4 µm. Even though the X-rays are more likely to be created closer to the beam than on the edge of the interaction volume, it would be problematic to use an interaction volume larger than the features we want to study. For this reason, we opted to use a lower energy of the primary beam (10 keV) with a calculated interaction volume with a diameter of 500 nm. Even though the Lα have similar energies, it is possible to separate them, but it may lead to higher error in the composition of Nb and Zr. We decided to perform a line scan through multiple regions to further minimize the error.

The apparent thickness of the β phase in the studied surface was around 0.1-0.2 µm. To maximize the precision of the chemical composition measurement, a location with a high amount of β phase was analyzed, see figure 4.13. The locations with high amounts of β usually contained small dark particles. We performed two line scans, the first one through β phase only and the second one through β phase with dark particles. From the ends of the first line scan (see figure 4.13), we determined that the α contains mainly zirconium and aluminum. Niobium was not detected in the α phase (see table 4.4). We determined the composition of β from the plateau between points 7 and 11 in figure 4.13. We detected high niobium content in the β phase 16 wt%. We measured a lower content of Zr and Al in comparison with the α (see table 4.4).

We performed the second line scan through the β phase with dark particles (see figure 4.14). It is evident that these regions are richer in zirconium and contain less niobium. For comparison with the first line scan, we calculated the composition of α from the first 5 points in this scan (see table 4.4). The results differ slightly from the first scan, but the results are within the range of error of both measurements. We can conclude that the α contains mainly zirconium

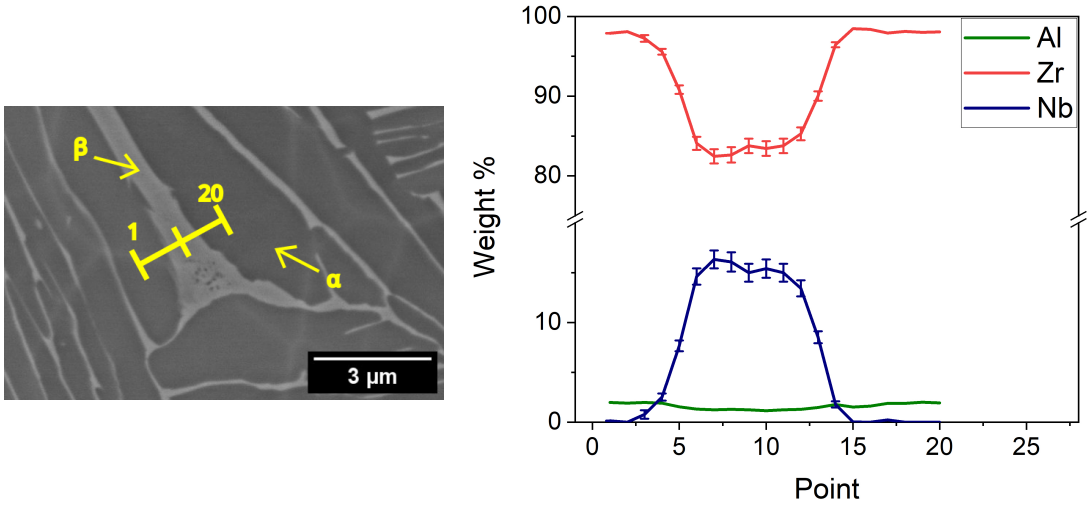

Figure 4.13 BSE image and results of EDX line scan performed on the initial state of Zr-4Nb-2Al.

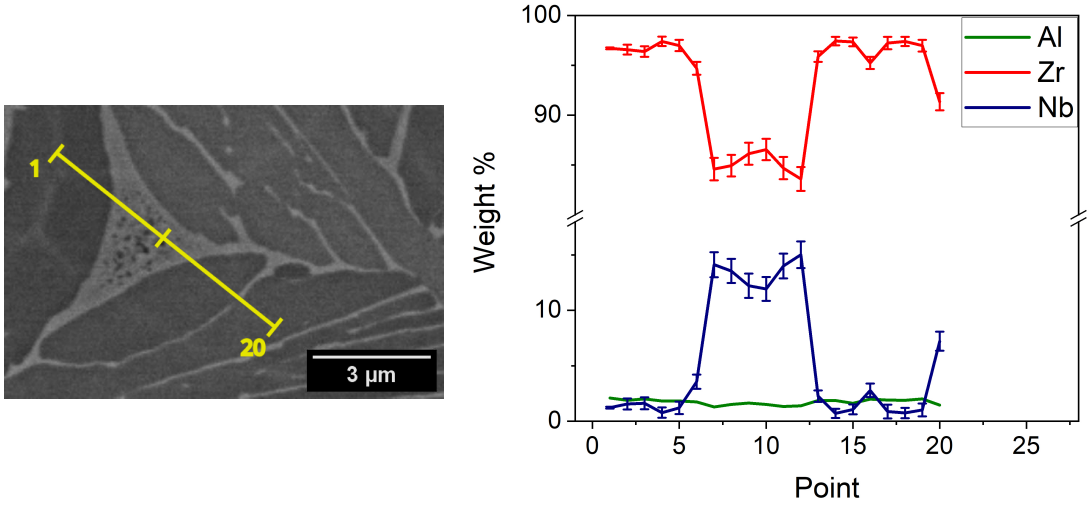

Figure 4.14 BSE image and results of EDX line scan through β phase with dark particles performed on the initial state of Zr-4Nb-2Al.

and aluminum and that most of the niobium is in the β phase. When analyzing EDX results, it is essential to remember that the interaction volume for X-rays is larger than for back-scattered and secondary electrons. Therefore, the EDX analysis results might not always correlate perfectly with an SEM image because under the surface visible in the SEM image, there might be a different composition that influences the EDX results.

4.3.3 Conclusion to initial state characterisation

In this section, we investigated the phase composition and microstructure of the studied Zr-4Nb-2Al alloy. We detected the presence of hcp α and bcc β. Fine microstructure of these phases was investigated by scanning electron microscopy. We measured the chemical composition of these phases by energy-dispersive X-ray spectroscopy. From the analysis we concluded that almost all niobium in the alloy is present in the β phase. This is in accordance with the Nb-Zr phase diagram (figure 1.9), which at low temperatures predicts a niobium-rich β phase.

4.4 Temperature evolution of phase composition in Zr-4Nb-2Al

In this section, we investigated the phase composition of Zr-4Nb-2Al in the same way as that of the alloy Zr-4Sn-1Cr, with the aim of studying the evolution of intermetallic phases present in the alloy. In situ DSC and resistometry measurements were performed, followed by postmortem SEM and XRD on the heat-treated samples. The author already investigated this alloy in his bachelor thesis [54], where he used DSC and resistivity measurements to investigate the $\alpha \rightarrow \beta$ transformation. In the next section, the resistivity measurement during heating is discussed, taken from [54], and a new measurement during cooling is added, which was not previously presented. In this work, we conducted a new DSC experiment measurement both during heating and cooling.

4.4.1 DSC and electric resistance measurements

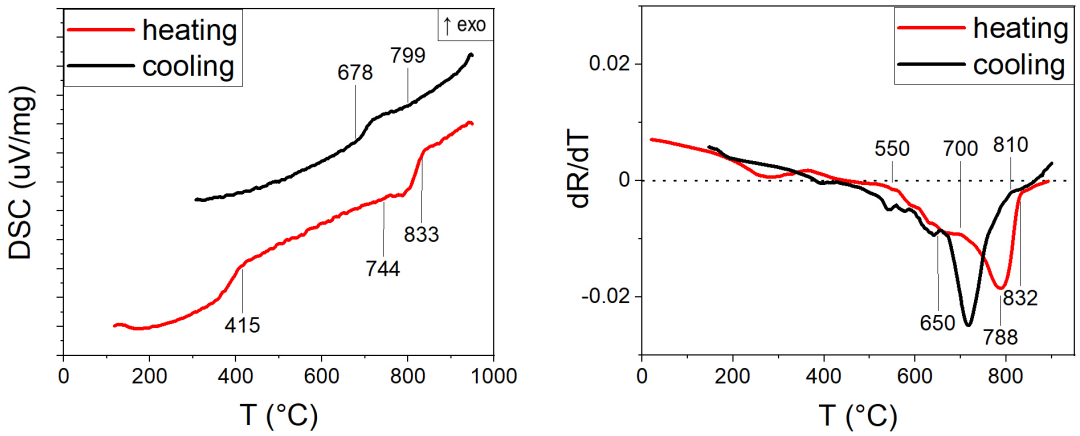

Figure 4.15 DSC and electric resistance measurements of Zr-4Nb-2Al.

The DSC curves during heating and cooling at a rate of 5 °C/min are presented in figure 4.15. At the start of heating, an endothermic process took place in the alloy, from 120 °C to 415 °C. In the next segment of the heating experiment, we observed another endothermic effect, detected as an endothermic peak from 744 °C to 833 °C. In previous work [54], the author already determined that the alloy undergoes the $\alpha \rightarrow \beta$ during this temperature range. During cooling, we detected this transformation as an exothermic peak from 678 °C to 799 °C. It is shifted to lower temperatures due to undercooling. After the end of $\alpha \rightarrow \beta$ at 835 °C, we observed no further process in the material.

The electric resistance measurement revealed more detailed information about the changes in the material. As in the case of the alloy Zr-4Sn-1Cr, the results are presented as the first derivative of electric resistance with respect to temperature (see figure 4.15). As we can see from the positive derivative at the beginning of the experiment, the resistance of the alloy steadily increased. At around 200 °C, we measured a decrease in the derivative. The cause for this may be the same as for the first endothermic peak in the DSC measurement. Both the observed endothermic peak and the decrease in the resistance derivative suggest a particular

phase dissolved during this process. In such a case, the decrease in the derivative can be explained as a dissolution of particles that acted as scattering centers for conduction electrons.

The resistance derivative reached zero value at 445 °C, indicating the maximum in electric resistance. After this temperature, the derivative maintained a stable value, and the electric resistance decreased steadily. Then, from 550 °C onward, the derivative rapidly decreased, appearing as two subsequent bends. The first bend took place from 550 °C to around 700 °C (which we measured as a rapid decrease in electric resistance). The second bend in resistivity had a minimum at 788 °C, after which the derivative increased and stabilized at 832 °C.

The measurement during cooling shows one prominent peak in the derivative between 650 °C and 810 °C where the resistivity of the sample increased rapidly with decreasing temperature. A similar bend in the derivative to the one in the heating experiment occurred at 650 °C.

According to the DSC and resistivity results, four annealing temperatures were chosen to explain the changes occurring in the Zr-4Nb-2Al alloy. Since we already examined the initial state, we chose the temperature 500 °C to investigate the changes during the first endothermic peak. We chose the temperatures of 610, 700, 820, and 850 °C to examine the material at different stages of the transformations detected between 550 °C and 835 °C. We heat-treated the alloy at these temperatures for one hour and quenched it in a water bath.

4.4.2 SEM and XRD

In this section, we study the alloy Zr-4Nb-2Al using the SEM and EDX methods. The alloy was heat treated at temperatures chosen in the previous section using the results from DSC and resistivity measurements. The first heat treatment we performed was at 500 °C. In the XRD analysis, we detected diffraction patterns of α and β phases (see figure 4.16). We detected well-defined peaks of both phases except for the reflection of {110} planes of bcc β, which was hidden behind the stronger reflections of {002} and {101} planes of the hcp α. From the integrated intensity of the peaks, we determined that the heat-treated material consisted of approximately 91 wt% α phase and 9 wt% β phase. This is a decrease in the content of β compared to the initial state, where we measured 13 wt% of β. However, it is reasonably within the error of the measurement, which consists of the error caused by the fitting and the local nature of the measurement.

We noticed no significant change in the microstructure when we examined the sample in the scanning electron microscope. As in the initial state (figure 4.17a), the heat-treated material comprised of α lamellae surrounded by the β phase. Representative pictures of the microstructure of the sample in in figure 4.17b.

Next, we performed a heat treatment at 610 °C to investigate the rapid decrease of resistivity, which we detected from 500°C onwards. We performed the XRD measurement of this sample and analyzed the given line profile. In addition to β and α phases, we detected the intermetallic Zr_2Al phase, which has a hexagonal structure of the P63/mmc space group. Only a few weak diffraction peaks of the Zr_2Al were detected. The diffractions from {100} and {101} were well visible at angles 9.6° and 11.8°, while the theoretically most

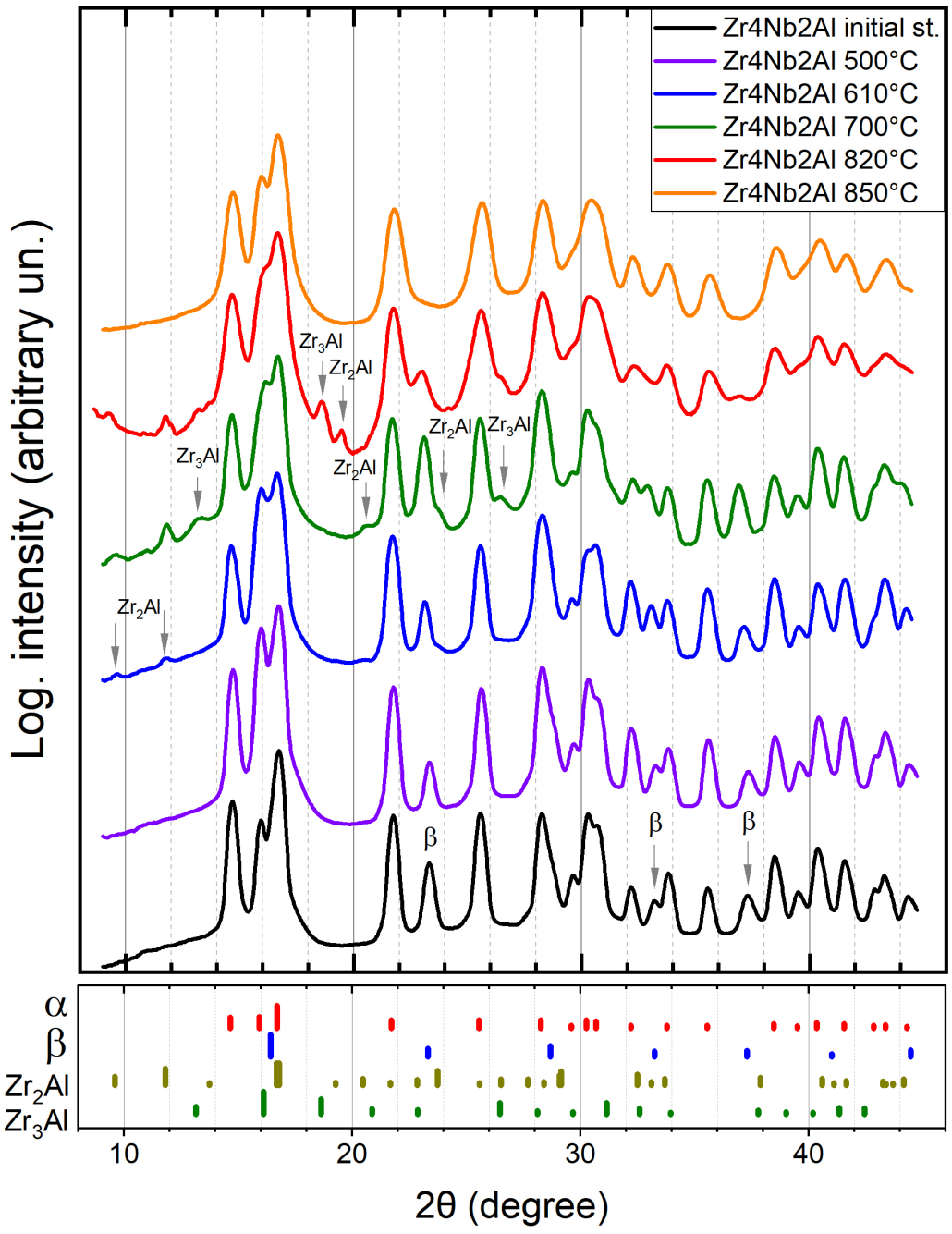

Figure 4.16 XRD line profiles of the initial and heat-treated states of Zr-4Nb-2Al.

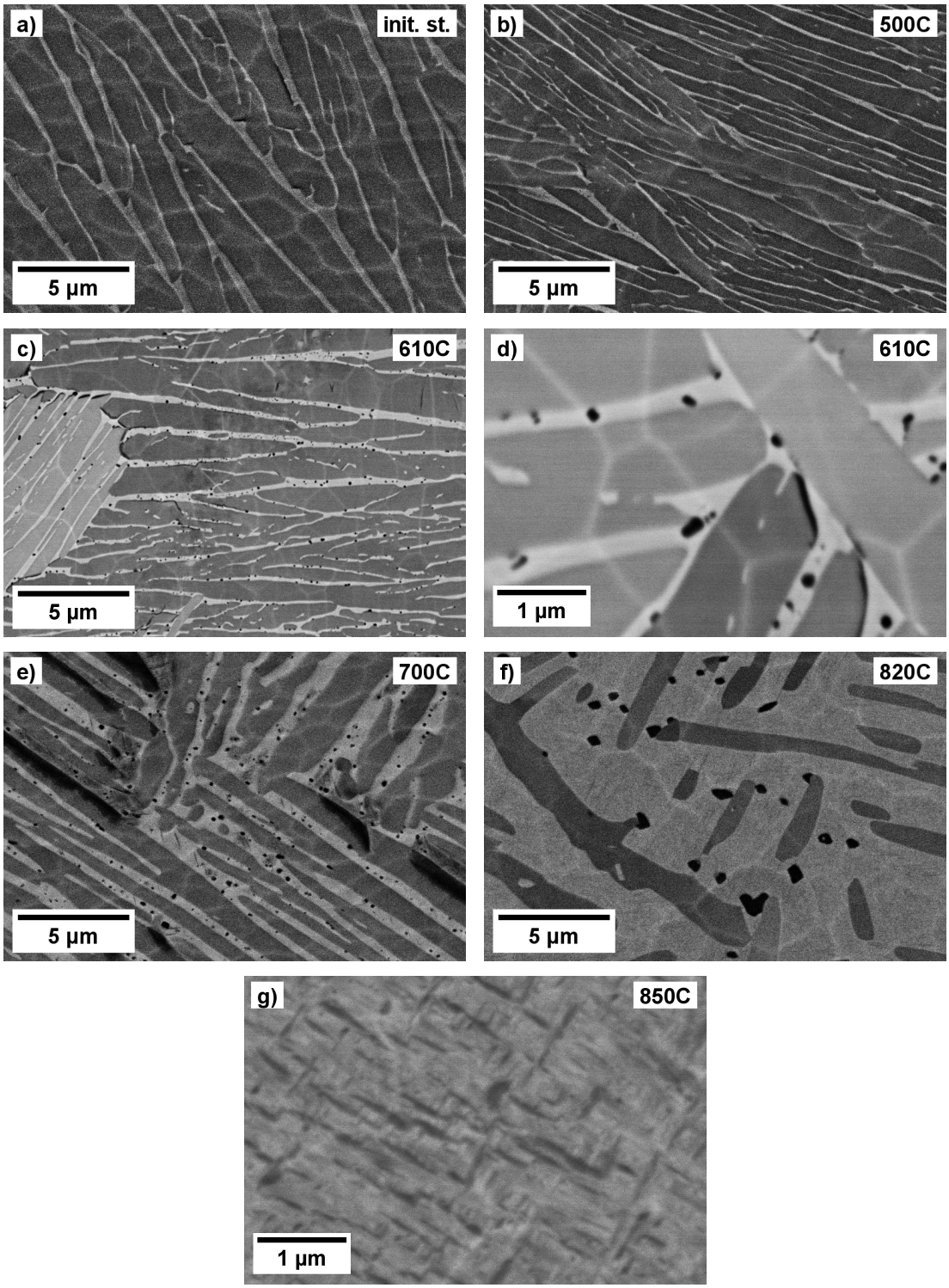

Figure 4.17 BSE images of alloy Zr-4Nb-2Al a) in the initial state, b-g) after different heat treatments.

intensive diffraction from the {110} planes at 16.7° was overlapped by the strong diffractions of the α and β phases. Other weaker peaks of the Zr_2Al were detected at 19.3°, 20.5° and 23.7°. Because of the weak peaks of the Zr_2Al, it was impossible to fit their intensities correctly. Thus, we performed the quantitative analysis only on the more intense peaks of the α and β phases and excluded the intermetallic phase. From the fit, we determined that 83.8 wt% of the material was the α phase and 16.2 wt% the β phase. This means that more β developed in the material during treatment at 610 °C compared to the sample heat-treated at 500 °C.

We also observed an increase in the fraction of the β phase and the precipitation of the intermetallic Zr_2Al in the scanning electron microscope. Figure 4.17c shows partially dissolved α and a larger amount of β phase. The intermetallic Zr_2Al particles can be observed as black dots embedded in the β phase in figure 4.17d. Aluminum is an α stabilizing element, and as it was verified by EDX measurements in chapter 4.3, it has a higher affinity to form a solid solution with the hcp α phase. This means that when the transformation $\alpha \rightarrow \beta$ occurred, high amounts of aluminum were released from the dissolving α phase, which then formed an intermetallic phase Zr_2Al. Interestingly, from the equilibrium binary phase diagram Zr-Al (figure 1.7), it follows that for the alloy with less than 33.3 at.% (or 9 wt%) the intermetallic phase Zr_3Al should be present in the alloy instead of the detected Zr_2Al. This prediction is only true in a binary alloy; for this reason, we simulated equilibrium phase composition for the exact Zr-4Nb-2Al (wt%) composition in a Thermo-Calc program. This simulation also predicted that in equilibrium, the Zr_3Al phase should be present in the material. Specifically, it should be present from low temperatures up to 688 °C, while the Zr_2Al should be stable from 688 °C to 781 °C. Both predictions say that the Zr_3Al intermetallic phase should form in the alloy instead of the measured Zr_2Al phase. This disagreement may be explained by the fact that the release of aluminum during $\alpha \rightarrow \beta$ creates a higher local concentration of aluminum, favoring the formation of the aluminum richer Zr_2Al hexagonal phase.

We performed further heat treatment at 700 °C, which is the start temperature of the second rapid decrease in resistivity. From the XRD analysis, we concluded that all previous phases were present in the alloy: α, β, and Zr_2Al. In addition, the intermetallic phase Zr_3Al was present in the material, which is a cubic phase of the $Pm\bar{3}m$ space group, identified by peaks at 13.2° and 26.5° corresponding to the 110 and 220 planes, respectively. For the same reason as above, we analyzed the quantitative phase composition only for the α and β phases. Compared with the previous samples, the fraction of β increased to 20.4 wt%.

BSE image of the state heat treated at 700 °C is in figure 4.17e. We can see further thinning of the α lamellae and the intermetallic particles of Zr_2Al still present in the β phase. Larger dark particles are visible in figure 4.17e at boundaries between the α and β phases.

Next, we studied the alloy after heat treatment at 820 °C. This temperature is within the endothermic peak detected in DSC measurement and within the second peak in resistivity measurement (figure 4.15). The β transus temperature, which is the temperature at which all of the α phase transforms to the β phase, is at 831±2 °C for the alloy Zr-4Nb-2Al [54]. This means that after annealing at the chosen temperature, most of the original hcp α should transform to the bcc β phase. From the x-ray diffraction, we determined that there was no change

in the phases present in the sample compared to the previous heat treatment (700 °C); α, β and intermetallic Zr_2Al and Zr_3Al. We analyzed the XRD line profile (see figure 4.16) and indexed three peaks belonging to the Zr_3Al intermetallic phase, one distinctive peak at 18.6° which belongs to the {200} planes and less visible peaks at 13.2° and 26.5° which belong to {110} and {320} planes, respectively. For the cubic Zr_2Al we identified well defined peaks belonging to {100}, {101} and {200} planes and one less visible peak from {202} planes.

The quantitative analysis performed on the XRD profile revealed that the volume fraction of the α and β phase was 88.7 wt% and 11.3 wt%, respectively. Note that the volume fraction of the β phase decreased compared to the previous heat treatment at 700 °C. The material would be expected to contain more β phase than after the heat treatment at 700 °C, because with the increasing temperature, it is energetically favorable for the material to contain more bcc β phase. However, as stated in [11], zirconium alloys undergo martensitic transformation to hexagonal or orthorhombic martensite when quenched from above the martensite start temperature. The martensite start temperature is below the β transus for elemental zirconium and further decreases for more β stabilized alloys [8]. Whether any β phase is retained after the quench is determined by the martensite finish temperature. In this case, a portion of the initial β was retained after the quench; this means that the martensite finish temperature for the β phase after the anneal lays below the temperature of the quenching bath, which was 20 °C in our case.

The α' martensite has the same crystal structure as the equilibrium α but different composition since it forms from the β phase by a martensitic transformation, not by nucleation and growth. Because of that, the diffraction line profile of the α and α' is the same and only slightly shifted from each other due to the difference in lattice parameters. This led to the broadening of hcp peaks in the measured XRD line spectrum (see figure 4.16).

The fact that during the heat treatment, more than 11.3 wt% of the alloy was the bbc β is captured in the images from scanning electron microscope (see figure 4.18a). The BSE signal primarily gives contrast based on the chemical composition, meaning that there is little to no contrast between the original β and the transformed α' martensite since they have the same composition. We analyzed the image by the color threshold in the ImageJ program, which divides the pixels of the image based on their brightness. This gave us a rough estimate that during the heat treatment (820 °C), the material contained around 50 % β phase.

In figure 4.17f, we can see dark intermetallic particles and large regions of transformed β phase. These particles formed preferentially near the β grain boundaries, as can be seen in figure 4.18a. Almost no intermetallic particles were present further inside the β grains. Since the size of the β grains was of the order of millimeters, there were areas in the scale of 100 µm without any intermetallic particles. This inhomogeneous distribution of intermetallic particles proved to be an obstacle for the previously discussed x-ray diffraction. The x-ray beam had a diameter of 0.3 mm; therefore, there was an insufficient amount of intermetallic particles in some measured regions. For this reason, multiple measurements had to be performed in various locations to obtain diffraction signal from both intermetallic phases. The line profile presented in figure 4.16 was measured in such a region where both intermetallic phases were present. The fractions of the α and

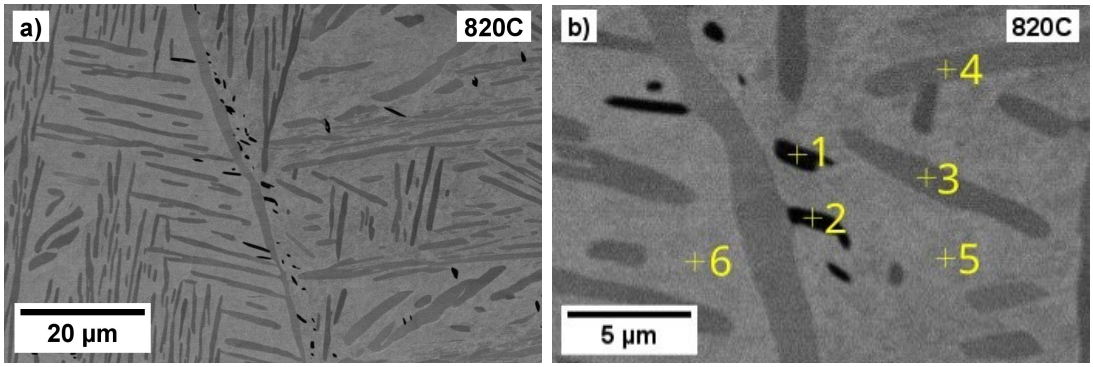

Figure 4.18 BSE images of EDX analysis of the Zr-4Nb-2Al alloy. a) Boundary between β grains. b) Close-up image of the EDX analysis.

β phases discussed above were calculated from this line profile.

We performed the EDX analysis of the α, β and intermetallic phases near the grain boundary (see figure 4.18a). We measured the x-ray spectra at selected points (marked by crosses in figure 4.18b) with an acceleration voltage of 5 keV. The analysis results are presented in table 4.5. As it was explained in chapter 4.3.2, the majority (16 wt%) of the Nb in the initial state was incorporated in the β phase. During the heating of the sample and the subsequent heat treatment, the α phase patially transformed to the β phase. After heat treatment, the β phase contained Zr and Al atoms which were released during the dissolution of the α phase. This effectively lowered the content of Nb in the β phase to 4.4 wt%. The lower stabilization of the β phase led to less of the β being retained after the quench.

		Weight frac. (%)	Atomic frac. (%))
spot 1	Al	7.8	22.3
	Zr	92	77.2
	Nb	0.6	0.5
spot 2	Al	7.3	20.9
	Zr	92.1	78.6
	Nb	0.6	0.5
spot 3	Al	1.8	5.8
(α)	Zr	98.0	94.0
	Nb	0.2	0.2
spot 4	Al	1.7	5.6
(α)	Zr	97.9	94
	Nb	0.4	0.4
spot 5	Al	1.3	4
(β)	Zr	94.4	92
	Nb	4.3	4
spot 6	Al	1.4	4.6
(β)	Zr	94.2	91.2
	Nb	4.4	4.2

Table 4.5 Results of EDX analysis performed on Zr-4Nb-2Al alloy heat-treated at 820 °C.

The last heat treatment we performed was at 850 °C, beyond the previously

determined β transus. In this state, no β or intermetallic phase were retained after the quenching, as it can be seen from the measured XRD line profile in figure 4.16. The intermetallic particles dissolved into the β phase during the heat treatment, which then transformed into the α' martensite during the quench. This resulted in a microstructure consisting of fine martensitic plates without any original α lamellae (see figure 4.17g).

4.4.3 Discussion of the phase composition evolution

Figure 4.19 shows the lattice parameters of the α and β phases after different heat treatments. The data for the initial state are denoted as "IS". Due to the same crystal structure of the α and α' martensite, we could not distinguish the peaks of the individual phases. This means that in cases where the α' was present, we calculated the lattice parameters from the contributions of both phases. In figure 4.19, we see the increase in the cubic β lattice parameter with increasing temperatures. With increasing temperature, the hexagonal structure of α displays a decreasing tendency in the c lattice parameter. The α lattice parameter increased after 700 °C and 820 °C treatments compared to the initial state.

The weight fractions of α+α' and β phases obtained by the XRD are shown in figure 4.20. After heat treatment at 500 °C, we measured a decrease to 9 wt% β compared to the initial state (13 wt%). We determined this decrease to be an effect caused by the local composition and the error of the measurement. After heat-treatments at 610 °C and 700 °C the fraction of β increased. In the state after treatment at 700 °C we observed the precipitation of intermetallic Zr_2Al phase from the β phase. The fraction of β observed after treatment at 820 °C decreased due to martensitic transformation to α'. Intermetallic particles of Zr_2Al and Zr_3Al were observed in this state. In the sample heat-treated at 850 °C, no β was retained, and we observed a fully martensitic microstructure without any intermetallic phases.

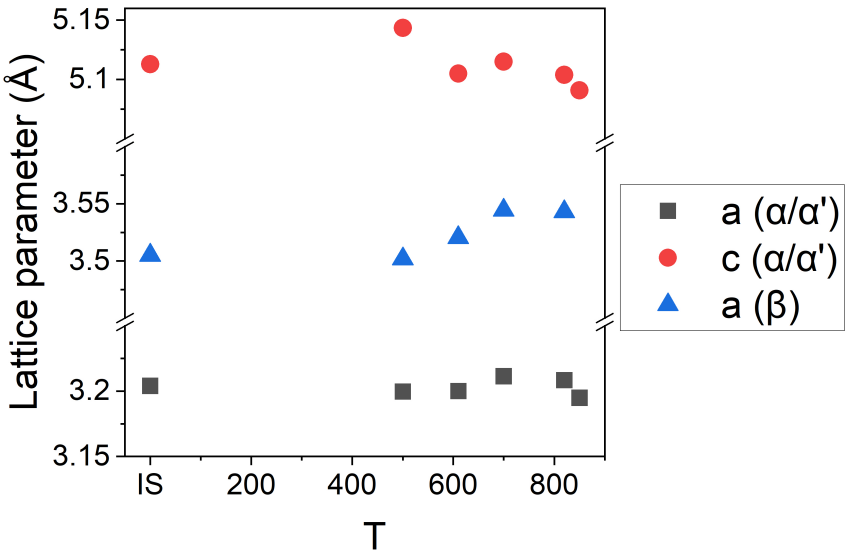

Figure 4.19 Lattice parameters obtained by XRD analysis of phases present in Zr-4Nb-2Al after different heat treatments.

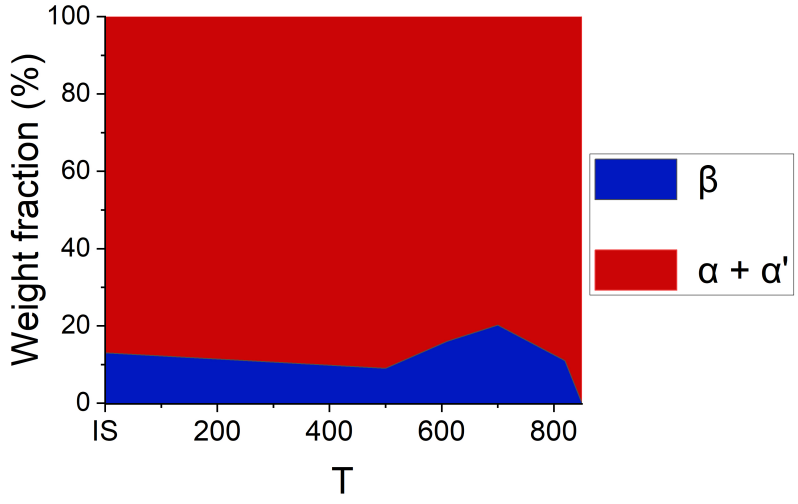

Figure 4.20 Phase composition of Zr-4Nb-2Al after different heat treatments.

4.5 Mechanical properties after thermomechanical treatment

After we investigated the phase composition and microstructure of the alloys, we performed thermomechanical treatment of the alloys by hot swaging. The swaging was done at two temperature steps: in the β region above the β transus and below the β transus in the $\alpha + \beta$ region. From the results in chapter 4.2 we determined the ideal temperature range for the $\alpha + \beta$ swaging of the Zr-4Sn-1Cr alloy to be 850-950 °C. For the swaging in the β region, we determined the temperature range of 1000-1200 °C. From the results in chapter 4.4 we determined the ideal temperature range for the $\alpha + \beta$ and β swaging of the Zr-4Nb-2Al alloy to be 600-800 °C and 850-1200 °C, respectively.

Both alloys were successfully swaged in the β phase field at temperatures between 1000-1200°. However, due to insufficient control of the feeding rate and the induction heating, both alloys were swaged in the temperature range of 600-800 °C in the next step. Resulting in the alloy Zr-4Nb-2Al being successfully forged in the $\alpha + \beta$ field, while the alloy Zr-4Sn-1Cr was forgedbelow the ideal range at temperatures in the α phase region.

4.5.1 Microstructure after swaging

We investigated the microstructure of the swaged alloys using SEM. The samples were cut from the rods in the transverse direction. The microstructure of Zr-4Sn-1Cr after the swaging consisted of α grains of the apparent diameters ranging from submicron sizes to a few µm (see figure 4.21a). We observed crystals of $ZrCr_2$ phase similar in size to those in the initial state investigated in chapter 4.1 (see figure 4.21b). We performed an XRD measurement and, from the line profile in figure 4.22, calculated the fractions of phases to be 98 wt% α and 2 wt% $ZrCr_2$.

The microstructure of the alloy Zr-4Nb-2Al consisted of small lamellar α grains with the apparent thickness below 150 nm (see figure 4.21c). The XRD measurement (see figure 4.22) showed the presence of α phase and Zr_2Al intermetallic phase, which precipitated during the forging in the $\alpha+\beta$ phase region. The lattice parameters considerably decreased compared with the initial state (see table 4.6). We identified no peaks from the β phase, possibly due to the change in the lattice parameter of the α phase, which shifted the stronger α reflections on top of the β reflections.

Zr-4Sn-1Cr	a_α (Å)	b_α (Å)	c_α (Å)
Initial state	3.223	3.223	5.150
Hot swaged state	3.222	3.222	5.149
Zr-4Nb-2Al	a_α (Å)	b_α (Å)	c_α (Å)
Initial state	3.204	3.204	5.113
Hot swaged state	2.950	2.950	4.686

Table 4.6 Comparison of α phase lattice parameters between initial and hot swaged states.

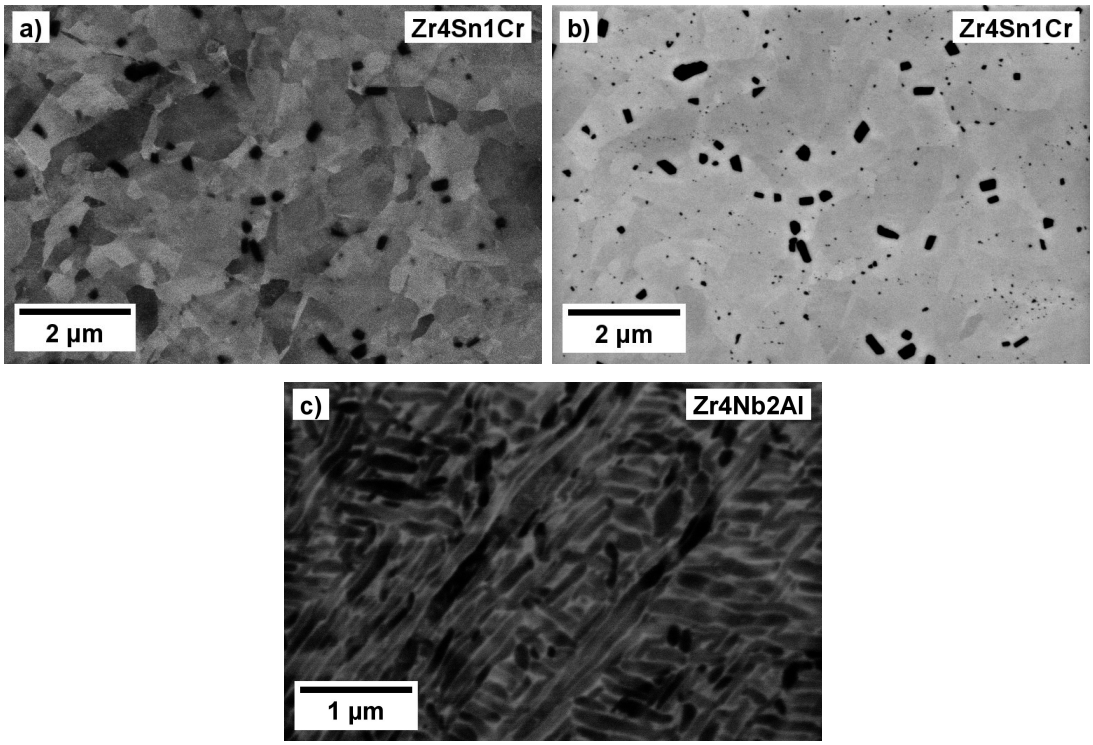

Figure 4.21 SEM microstructure images of hot swaged alloys. a) BSE image of Zr-4Sn-1Cr alloy. b) Low energy SE image of Zr-4Sn-1Cr. c) BSE image of Zr-4Nb-2Al.

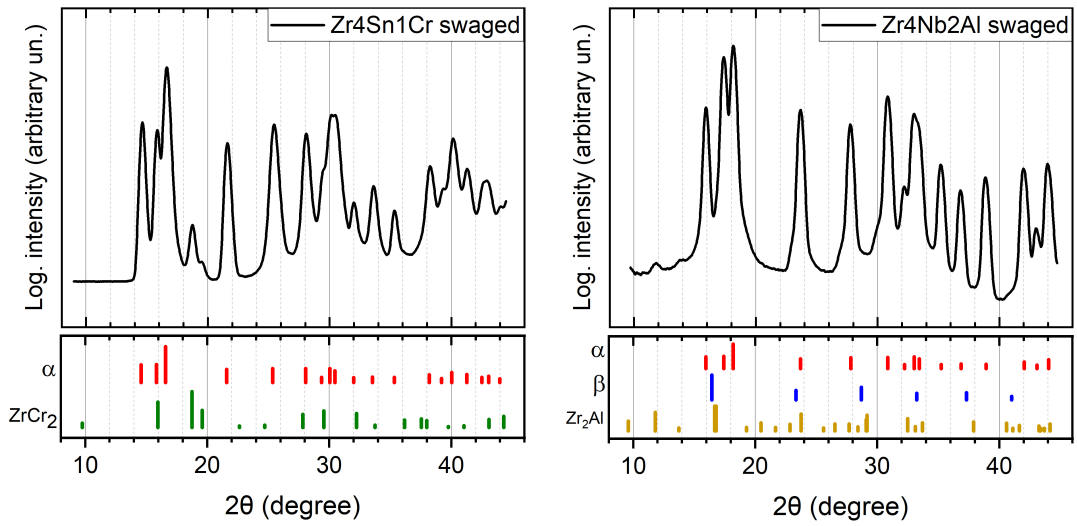

Figure 4.22 The XRD line profiles of hot swaged Zr-4Sn-1Cr and Zr-4Nb-2Al alloys.

Zr-4Sn-1Cr	HV	Error
Initial st.	180	10
Hot swaged st. (longitudinal)	269	3
Hot swaged st. (transverse)	251	2
Zr-4Nb-2Al	HV	Error
Initial st.	240	10
Hot swaged st. (longitudinal)	296	5
Hot swaged st. (transverse)	190	6

Table 4.7 Results of the Vickers microhardness tests.

Alloy	Ductility (%)	$\sigma_{0.2}$ (MPa)	σ_{UTS} (Mpa)	E (GPa)
Zr-4Sn-1Cr	14	533	897	46
Zr-4Nb-2Al	13.7	509	944	42
Zircaloy (stress relieved)	18	570	770	

Table 4.8 Results of tensile tests of hot swaged Zr-4Sn-1Cr and Zr-4Nb-2Al alloys compared to mechanical properties of commercial Zircaloys [55].

4.5.2 Tensile and microhardness tests

We performed Vickers microhardness measurements on the swaged and initial states of both alloys. Due to the possible anisotropy of the swaged samples, we investigated the microhardness of samples cut in two different directions. The first set of samples was cut in the longitudinal direction and the second in the transverse direction (as described in chapter 3.1.1). The measurement results are in table 4.7. In the Zr-4Sn-1Cr alloy, the microhardness differs slightly between the longitudinal and transverse samples. We measured a substantial increase in microhardness between the initial and swaged samples. This is due to the fine microstructure of sub-micron grains in the swaged samples (figure 4.21a), which impede the dislocation motion more than the large grains observed in the initial state (figure 4.2).

In the case of the Zr-4Nb-2Al alloy, we measured a substantial difference in microhardness in the longitudinal and transversal directions. The measured microhardness was more than 100 HV higher in the longitudinal plane than in the transversal plane, indicating large anisotropy in mechanical properties. The longitudinal sample (296 HV) achieved higher microhardness than the initial state (240 HV), which we attribute to the decrease in the α grain size.

We performed tensile tests on both swaged alloys. The measured true stress-true strain curve is in figure 4.23, and the results of the tensile tests compared with typical mechanical properties of commercial thermo-mechanically processed Zircalloys (Zircaloy-2 and Zircaloy-4) are in table 4.8.

Compared to the commercial Zircaloys, both alloys Zr-4Sn-1Cr, and Zr-4Nb-2Al achieved higher ultimate tensile strength, lower yield strength, and lower ductility. According to [55], the ductility of the forged alloys might be increased by stress relieving annealing, which is performed for Zircaloys at 480 °C for 4 hours followed by slow cooling.

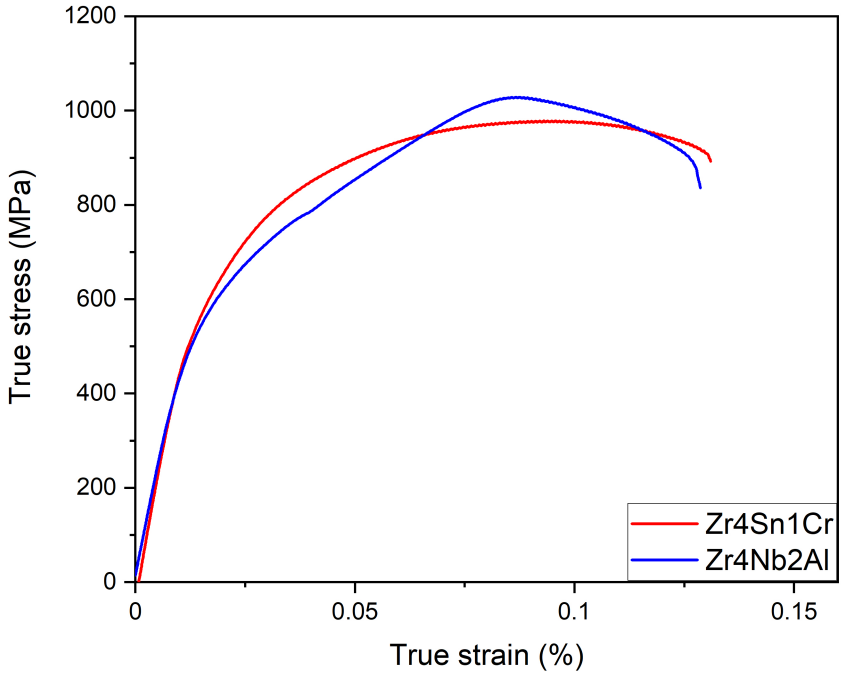

Figure 4.23 True stress-true strain curve of hot swaged Zr-4Sn-1Cr and Zr-4Nb-2Al alloys.

Conclusion

This work focused on the characterization of two newly developed zirconium alloys, Zr-4Sn-1Cr and Zr-4Nb-2Al. In the first part, we focused on the microstructure and phase composition of the studied alloys.

- In the alloy Zr-4Sn-1Cr, we determined the presence of hcp α and intermetallic $ZrCr_2$ phases in the initial state and after heat-treatments at various temperatures (500-940 °C) using XRD analysis. In SEM, we observed the evolution in the microstructure of the $ZrCr_2$ particles between the initial state and heat-treatments at 500 °C and 700 °C.

- In the initial state of the second alloy, Zr-4Nb-2Al, we observed $\alpha + \beta$ microstructure, consisting of fine α lamellae in the β matrix. We observed zirconium-rich particles which were present in the β phase. We heat-treated the alloy at temperatures between 500 °C and 850 °C. After the heat treatment at 610 °C, we observed the precipitation of intermetallic Zr_2Al particles. The Zr_2Al particles were distributed in the β phase and at boundaries between α and β phases. In addition to Zr_2Al, the presence of Zr_3Al phase was determined in samples heat-treated at 700 °C and 820 °C. After heat treatment at 850 °C, we observed a microstructure fully consisting of α' martensite with no intermetallic phases being present.

In the second part, we determined the ideal parameters for the hot swaging based on the phase composition investigation and performed β swaging followed by α swaging of the Zr-4Sn-1Cr and β swaging followed by $\alpha + \beta$ swaging of the Zr-4Nb-2Al alloy. We then investigated the microstructure and mechanical properties by microhardness measurements and tensile tests.

- The microstructure of Zr-4Sn-1Cr swaged in the β and α phase regions consisted of α grains of the apparent diameters ranging from submicron sizes to a few µm and $ZrCr_2$ particles. We measured a substantial increase in the microhardness of the swaged material in both the longitudinal (259 HV) and the transverse (251 HV) samples in comparison with the 180 HV of the initial state.

- We observed small lamellar α grains of thickness below 150 nm in the hot swaged Zr-4Nb-2Al. The presence of intermetallic Zr_2Al, which formed during the $\alpha + \beta$ swaging, was determined by XRD analysis. The microhardness of swaged Zr-4Nb-2Al showed considerable difference between the longitudinal (296 HV) and transverse (190 HV) samples, which had lower microhardness than the initial state (240 HV).

- Both hot-swaged Zr-4Sn-1Cr and Zr-4Nb-2Al alloys showed higher ultimate tensile stress of 897 MPa and 944 MPa, respectively, compared to commercial thermo-mechanically processed Zircaloy-2 and Zircaloy-4 (770 MPa).

Future work will include further research on the thermomechanical processing of zirconium alloys:

- Research and design of optimal heat treatment of the hot-swaged alloys, including recrystallization and stress-relieving annealing. It is probable that the optimal heat treatment will differ from the usual treatment of low-alloyed zirconium alloys.
- Repeat the hot swaging of Zr-4Sn-1Cr correctly in $\alpha + \beta$ and β phase fields and study the differences in microstructure and mechanical properties with the β and α swaged state.

Additionally, future work will focus on further study of the phase composition of Zr-4Nb-2Al:

- Determine the presence of β phase in the hot-swaged Zr-4Nb-2Al alloy using transmission electron microscopy (TEM) since the investigation by XRD was inconclusive.
- Study the zirconium-rich particles present in the initial state by TEM. The dissolution of these particles is the probable cause of the first endothermic peak observed in the DSC measurement.

Bibliography

1. Zhao, Qian; Ueno, Takeshi; Wakabayashi, Noriyuki. A review in titanium-zirconium binary alloy for use in dental implants: Is there an ideal Ti-Zr composing ratio? *Japanese Dental Science Review*. 2023, vol. 59, pp. 28–37. ISSN 1882-7616. Available from DOI: https://doi.org/10.1016/j.jdsr.2023.01.002.
2. Milošev, I; Frankel, GS. Conversion coatings based on zirconium and/or titanium. *Journal of The Electrochemical Society*. 2018, vol. 165, no. 3, pp. C127–C144.
3. Jing, R; Liang, SX; Liu, CY; Ma, MZ; Zhang, XY; Liu, RP. Structure and mechanical properties of Ti–6Al–4V alloy after zirconium addition. *Materials Science and Engineering: A*. 2012, vol. 552, pp. 295–300.
4. Schemel, JH. *Zirconium in the Nuclear Industry*. ASTM International, 1979.
5. Duan, Zhengang; Yang, Huilong; Satoh, Yuhki; Murakami, Kenta; Kano, Sho; Zhao, Zishou; Shen, Jingjie; Abe, Hiroaki. Current status of materials development of nuclear fuel cladding tubes for light water reactors. *Nuclear Engineering and Design*. 2017, vol. 316, pp. 131–150. ISSN 0029-5493. Available from DOI: https://doi.org/10.1016/j.nucengdes.2017.02.031.
6. Semiatin, S. L. An Overview of the Thermomechanical Processing of α/β Titanium Alloys: Current Status and Future Research Opportunities. *Metallurgical and Materials Transactions A* [online]. 2020, vol. 51, no. 6, pp. 2593–2625 [visited on 2024-04-21]. ISSN 1073-5623, ISSN 1543-1940. Available from DOI: 10.1007/s11661-020-05625-3.
7. Ding, R.; Guo, Z.X.; Wilson, A. Microstructural evolution of a Ti–6Al–4V alloy during thermomechanical processing. *Materials Science and Engineering: A*. 2002, vol. 327, no. 2, pp. 233–245. ISSN 0921-5093. Available from DOI: https://doi.org/10.1016/S0921-5093(01)01531-3.
8. Banerjee, S.; Mukhopadhyay, P. *Phase transformations: examples from titanium and zirconium alloys*. Amsterdam ; Oxford: Elsevier/Pergamon, 2007. Pergamon materials series, no. 12. ISBN 978-0-08-042145-2.
9. Dornelf. Hexagonal close packed (hcp) unit cell. *Wikimedia Commons* [online]. [N.d.] [visited on 2022-05-06]. Available from: https://commons.wikimedia.org/wiki/File:Hexagonal_close_packed.png.
10. Mayer, Daniel. Body-centered cubic crystal structure. *Wikimedia Commons* [online]. [N.d.] [visited on 2022-05-06]. Available from: https://commons.wikimedia.org/wiki/File:Cubic-body-centered.svg.
11. Banerjee, S; Krishnan, R. Martensitic transformation in zirconium-niobium alloys. *Acta Metallurgica*. 1971, vol. 19, no. 12, pp. 1317–1326. ISSN 0001-6160. Available from DOI: https://doi.org/10.1016/0001-6160(71)90068-X.
12. Lütjering, G.; Williams, J. C. *Titanium*. 2nd ed. Berlin ; New York: Springer, 2007. Engineering materials and processes. ISBN 978-3-540-71397-5.

13. Smallman, Raymond Edward. *Modern physical metallurgy*. Elsevier, 2016.

14. Hume-Rothery, William. *Researches on the nature, properties, and conditions of formation of intermetallic compounds, with special reference to certain compounds of tin*. 1926. PhD thesis. University of London.

15. Magruder, Benjamin R; Dorfman, Kevin D. The C36 Laves phase in diblock polymer melts. *Soft Matter*. 2021, vol. 17, no. 39, pp. 8950–8959.

16. Okamoto, H. *J. Phase Equilib.* 1993, vol. 14, p. 768.

17. Arias, D; Abriata, JP. The Cr- Zr (chromium-zirconium) system. *Bulletin of Alloy Phase Diagrams*. 1986, vol. 7, no. 3, pp. 237–244.

18. Bumball, W.M. Phase equilibria in zirconium-rich zirconium-chromium-oxygen alloys. *Less-Common Metals*. 1969, no. 19, p. 345.

19. Keys, L.H. The physical metallurgy of high strength zirconium alloys. *Jurnal of Nuclear Materials*. 1976, no. 59, p. 137.

20. Jung, Yang-Il; Seol, Yong-Nam; Choi, Byoung-Kwon; Park, Jeong-Yong; Jeong, Yong-Hwan. Effect of Cr on the creep properties of zirconium alloys. *Journal of Nuclear Materials*. 2010, vol. 396, no. 2, pp. 303–306. ISSN 0022-3115. Available from DOI: https://doi.org/10.1016/j.jnucmat.2009.10.058.

21. Couet, Adrien; Motta, Arthur T; Comstock, Robert J. Effect of alloying elements on hydrogen pick-up in zirconium alloys. In: *17th International Symposium on Zirconium in the Nuclear Industry, ASTM STP*. 2015, vol. 1543, pp. 479–514.

22. Okamoto, H. Sn-Zr (tin-zirconium). *Journal of phase equilibria and diffusion*. 2010, vol. 31, pp. 411–412.

23. Nam, Cheol; Kim, Kyeong-Ho; Lee, Myung-Ho; Jeong, Yong-Hwan. Effect of alloying elements on the thermal creep of zirconium alloys. *Nuclear Engineering and Technology*. 2000, vol. 32, no. 4, pp. 372–378.

24. Pahutová, M.; Kuchařová, K.; Čadek, J. Martensitic zirconium alloys: Influence of chemical composition on creep characteristics. *Journal of Nuclear Materials*. 1985, vol. 131, no. 1, pp. 20–31. ISSN 0022-3115. Available from DOI: https://doi.org/10.1016/0022-3115(85)90420-9.

25. Jerlerud Pérez, R.; Toffolon-Masclet, C.; Joubert, J.-M.; Sundman, B. The Zr–Sn binary system: New experimental results and thermodynamic assessment. *Calphad* [online]. 2008, vol. 32, no. 3, pp. 593–601 [visited on 2024-03-05]. ISSN 03645916. Available from DOI: 10.1016/j.calphad.2008.04.001.

26. Banerjee, S.; Mukhopadhyay, P. (eds.). Chapter 1 - Phases and Crystal Structures. In: *Phase Transformations*. Pergamon, 2007, vol. 12, pp. 1–86. Pergamon Materials Series. ISSN 1470-1804. Available from DOI: https://doi.org/10.1016/S1470-1804(07)80054-X.

27. Abriata, J. P.; Bolcich, J. C. The Nb-Zr (Niobium-Zirconium) system. *Journal of Phase Equilibria* [online]. 1982, vol. 3, no. 1, pp. 34–44 [visited on 2024-03-05]. ISSN 1054-9714. Available from DOI: 10.1007/BF02873409.

28. Hunt, C.E.L.; Niessen, P. The continuous cooling transformation behaviour of zirconium-niobium-oxygen alloys. *Journal of Nuclear Materials*. 1971, vol. 38, no. 1, pp. 17–25. ISSN 0022-3115. Available from DOI: https://doi.org/10.1016/0022-3115(71)90003-1.

29. Charit, I.; Murty, K.L. Creep behavior of niobium-modified zirconium alloys. *Journal of Nuclear Materials*. 2008, vol. 374, no. 3, pp. 354–363. ISSN 0022-3115. Available from DOI: https://doi.org/10.1016/j.jnucmat.2007.08.019.

30. Murray, J.; Peruzzi, A.; Abriata, J. P. The Al-Zr (aluminum-zirconium) system. *Journal of Phase Equilibria* [online]. 1992, vol. 13, no. 3, pp. 277–291 [visited on 2024-04-29]. ISSN 1054-9714. Available from DOI: 10.1007/BF02667556.

31. Potzschke, M.; Schubert, K. On the Construction of Some T4-B3 Homologous and QuasihomologousSystems. II. The Ti-A1, Zr-AI, Hf-A1, Mo-A1 and Some Ternary Systems. *Z.Metallkd.* 1962, vol. 53, pp. 548–561.

32. Lin, Xi-Heng; Beyerlein, Irene J.; Han, Wei-Zhong. Annealing cracking in Zr and a Zr-alloy with low hydrogen concentration. *Journal of Materials Science and Technology*. 2024, vol. 182, pp. 165–175. ISSN 1005-0302. Available from DOI: https://doi.org/10.1016/j.jmst.2023.09.039.

33. Kass, Stanley. *The development of the zircaloys*. 1962. Tech. rep. Westinghouse Electric Corp. Bettis Atomic Power Lab., Pittsburgh.

34. Cox, B. Some thoughts on the mechanisms of in-reactor corrosion of zirconium alloys. *Journal of Nuclear Materials*. 2005, vol. 336, no. 2, pp. 331–368. ISSN 0022-3115. Available from DOI: https://doi.org/10.1016/j.jnucmat.2004.09.029.

35. Sabol, GP. ZIRLO — An Alloy Development Success. *Journal of ASTM International*. 2005, vol. 2, no. 2, pp. 1–22. ISSN 1546-962X. Available from DOI: 10.1520/JAI12942.

36. Garde, A. M.; Comstock, R. J.; Pan, G.; Baranwal, R.; Hallstadius, L.; Cook, T.; Carrera, F. Advanced Zirconium Alloy for PWR Application. In: *Zirconium in the Nuclear Industry: 16th International Symposium*. ASTM International, 2012. ISBN 978-0-8031-7515-0. Available from DOI: 10.1520/STP152920120031.

37. Foster, John Paul; Yueh, H. Ken; Comstock, Robert J. ZIRLO Cladding Improvement. In: *Zirconium in the Nuclear Industry: 15th International Symposium*. ASTM International, 2009. ISBN 978-0-8031-4514-6.

38. Chakravartty, J. K.; Gupta, Chiradeep. Hot Working of Zirconium Alloys: Some Recent Developments. *Mineral Processing and Extractive Metallurgy Review* [online]. 2001, vol. 22, no. 1, pp. 197–220 [visited on 2024-03-14]. ISSN 0882-7508, ISSN 1547-7401. Available from DOI: 10.1080/08827509808962496.

39. Crewe, A. V.; Eggenberger, D. N.; Wall, J.; Welter, L. M. Electron Gun Using a Field Emission Source. *Review of Scientific Instruments*. 1968, vol. 39, no. 4, pp. 576–583. ISSN 0034-6748. Available from DOI: 10.1063/1.1683435.

40. Vernon-Parry, K.D. Scanning electron microscopy: an introduction. *III-Vs Review* [online]. 2000, vol. 13, no. 4, pp. 40–44 [visited on 2024-03-11]. ISSN 09611290. Available from DOI: 10.1016/S0961-1290(00)80006-X.

41. Choudhary, O.P.; Choudhary, Priyanka. Scanning Electron Microscope: Advantages and Disadvantages in Imaging Components. *International Journal of Current Microbiology and Applied Sciences*. 2017, vol. 6, pp. 1877–1882. Available from DOI: 10.20546/ijcmas.2017.605.207.

42. Wang, R. Progress in Nanoscale Characterization and Manipulation. In: Springer Singapore, 2018, pp. 35–68.

43. Wandrol, Petr; Vesseur, EJR; Vasina, Radovan; Ilitchev, Alex. Advanced SEM Imaging with the Trinity Detection System. [N.d.].

44. Luo, Zhiping. *A practical guide to transmission electron microscopy : fundamentals*. A practical guide to transmission electron microscopy : fundamentals. First edition. New York, [New York] (222 East 46th Street, New York, NY 10017): Momentum Press, 2016. Materials characterization and analysis collection. ISBN 1-60650-704-4.

45. Drouin, Dominique; Couture, Alexandre Réal; Joly, Dany; Tastet, Xavier; Aimez, Vincent; Gauvin, Raynald. CASINO V2.42—A Fast and Easy-to-use Modeling Tool for Scanning Electron Microscopy and Microanalysis Users. *Scanning* [online]. 2007, vol. 29, no. 3, pp. 92–101 [visited on 2024-03-25]. ISSN 0161-0457, ISSN 1932-8745. Available from DOI: 10.1002/sca.20000.

46. Vlasov, N. M.; Fedik, I. I. Hydrogen Embrittlement of Zirconium Alloys. *Metal Science and Heat Treatment*. 2003, vol. 45, pp. 328–331. Available also from: https://api.semanticscholar.org/CorpusID:134740399.

47. Jia, Yu-Jie; Han, Wei-Zhong. Mechanisms of Hydride Nucleation, Growth, Reorientation, and Embrittlement in Zirconium: A Review. *Materials* [online]. 2023, vol. 16, no. 6, p. 2419 [visited on 2024-03-20]. ISSN 1996-1944. Available from DOI: 10.3390/ma16062419.

48. Motta, Arthur T; Capolungo, Laurent. Hydrogen in zirconium alloys: A review. *Journal of Nuclear Materials*. 2019, vol. 518, pp. 440–460.

49. X-ray Single Crystal Structure Analysis System R-AXIS RAPID. *The Rigaku Journal*. 1998, vol. 15, no. 2.

50. Giannakopoulos, A.E.; Larsson, P.-L.; Vestergaard, R. Analysis of Vickers indentation. *International Journal of Solids and Structures*. 1994, vol. 31, no. 19, pp. 2679–2708. ISSN 0020-7683. Available from DOI: https://doi.org/10.1016/0020-7683(94)90225-9.

51. Buitrago, Juan; Ortega Portilla, Carolina; Mambuscay, Claudia; Piamba Jimenez, Jeferson; Forero, Manuel. Determination of Vickers Hardness in D2 Steel and TiNbN Coating Using Convolutional Neural Networks. *Metals*. 2023, vol. 13, p. 1391. Available from DOI: 10.3390/met13081391.

52. Banaszek, Grzegorz; Ozhmegov, Kirill; Kawalek, Anna; Sawicki, Sylwester; Magzhanov, Medet; Arbuz, Alexandr. Investigation of the Influence of Hot Forging Parameters on the Closing Conditions of Internal Metallurgical Defects in Zirconium Alloy Ingots. *Materials* [online]. 2023, vol. 16, no. 4, p. 1427 [visited on 2024-03-14]. ISSN 1996-1944. Available from DOI: 10.3390/ma16041427.

53. Veverková, A.; Harcuba, P.; Veselý, J. Sequence of phase transformations in metastable β Zr-12Nb alloy studied in situ by HEXRD and complementary techniques. *Journal of Materials Research and Technology* [online]. 2023, vol. 23, pp. 5260–5269 [visited on 2024-04-17]. ISSN 22387854. Available from DOI: 10.1016/j.jmrt.2023.02.076.

54. Strnad, Adam. Studium mikrostruktury a fázových transformací slitin zirkonia. 2022.

55. Lemaignan, C. Zirconium Alloys: Properties and Characteristics. In: *Comprehensive Nuclear Materials* [online]. Elsevier, 2012, pp. 217–232 [visited on 2024-04-22]. ISBN 978-0-08-056033-5. Available from DOI: 10.1016/B978-0-08-056033-5.00015-X.

List of Figures

List of Tables

List of Abbreviations

BSE	backscattered electrons
DSC	differential scanning calorimetry
EDX	energy dispersive spectroscopy
FEG	field emission gun
HV	Vickers hardness
SE	secondary electrons
SEM	scanning electron microscope
TEM	transmission electron microscope
XRD	X-ray diffraction